JACS Au
AN OPEN ACCESS JOURNAL OF THE AMERICAN CHEMICAL SOCIETY

pubs.acs.org/jacsau
Article

Insight into the Synergistic Effect of Binary Nonmetallic Codoped Co_3O_4 Catalysts for Efficient Ethyl Acetate Degradation under Humid Conditions

Fukun Bi, Jiafeng Wei, Zhuoxuan Zhou, Yaofei Zhang, Bin Gao, Ning Liu, Jingcheng Xu, Baolin Liu, Yuandong Huang, and Xiaodong Zhang*

Cite This: JACS Au 2025, 5, 363−380
Read Online

ACCESS | Metrics & More | Article Recommendations | Supporting Information

ABSTRACT: The synthesis of high-performance catalysts for volatile organic compounds (VOCs) degradation under humid conditions is essential for their practical industrial application. Herein, a codoping strategy was adopted to synthesize the N−Co_3O_4−C catalyst with N, C codoping for low-temperature ethyl acetate (EA) degradation under humid conditions. Results showed that N−Co_3O_4−C exhibited great catalytic activity (T_{90} = 177 °C) and water resistance (5.0 vol% H_2O, T_{90} = 178 °C) for EA degradation. Characterization results suggested that the C, N codoping weakened the Co−O bond strength, increased surface Co^{3+} and O_{ads} species, and improved the low-temperature redox ability and the mobility of lattice oxygen species, which boosted the catalytic performance of N−Co_3O_4−C for EA degradation. Meanwhile, the N-doping-induced oxygen vacancies could interact with water vapor to generate extra active oxygen species, which enhanced the water resistance. Importantly, based on a series of characterization technologies, in situ diffuse reflectance infrared Fourier transform spectroscopy (DRIFTS), and theoretical calculations, the synergistic effect of C, N codoping was systematically investigated and elucidated. The C doping induced the increase of surface area and the weakening of Co−O bond strength, which improved EA adsorption and lattice oxygen species activation to dissociate and oxidize EA, forming the key intermediate, acetate acid. N doping enhanced the adsorption and activation of gaseous oxygen species to form active oxygen species, attacking and breaking the C−C bond in acetate acid to accelerate EA deep oxidation, which synergistically facilitated EA degradation.

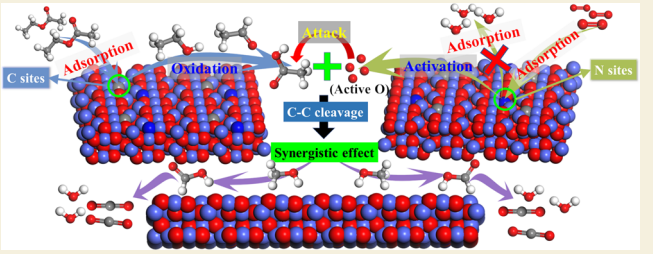

KEYWORDS: *catalytic oxidation, ethyl acetate degradation, synergistic effect, Co_3O_4 catalysts, C and N codoping*

1. INTRODUCTION

As one of the most essential atmospheric gaseous pollutants, volatile organic compounds (VOCs) have caused serious hazards to the environment and human health.[1,2] Oxygenated volatile organic compounds (OVOCs), such as ethyl acetate (EA), acetone, etc., as one kind of VOC, discharged from pharmaceutical, spray printing, and chemical manufacturing industries, are the main precursors for the formation of ozone and photochemical smog.[3,4] Therefore, it is significant to eliminate the emission of VOCs for green, sustainable development. At present, many technologies, such as adsorption,[5,6] photocatalysis,[7−9] plasma-catalysis,[10] photothermal catalysis,[11] and catalytic oxidation,[12−15] have been developed for VOC removal. Among them, catalytic oxidation with the preponderances of high efficiency, simple operation, and no secondary pollution has been considered one of the most hopeful technologies for VOC pollution treatment and widely applied.[16] Meanwhile, based on the catalytic oxidation technology, many catalysts, including supported noble metal catalysts[17] and transition metal oxide (TMO) catalysts,[18] have been studied for VOC degradation at low temperature. Therefore, because of their resourcefulness, effectiveness, and economic advantages, TMO catalysts have attracted extensive attention.

As a typical TMO catalyst, the Co_3O_4 catalyst with the spinel structure of AB_2O_4 is one of the most studied TMOs for VOC degradation.[19−21] For instance, Chen et al.[22] synthesized a series of Co_3O_4 catalysts with different exposed crystal planes for styrene complete oxidation, which presented excellent styrene degradation performance. Meanwhile, the high oxygen mobility, multiple oxidation states, weak Co−O bond strength, and the easy generation of highly active oxygen species also endowed the good VOC catalytic degradation performance to

Received: November 27, 2024
Revised: December 22, 2024
Accepted: December 26, 2024
Published: January 8, 2025

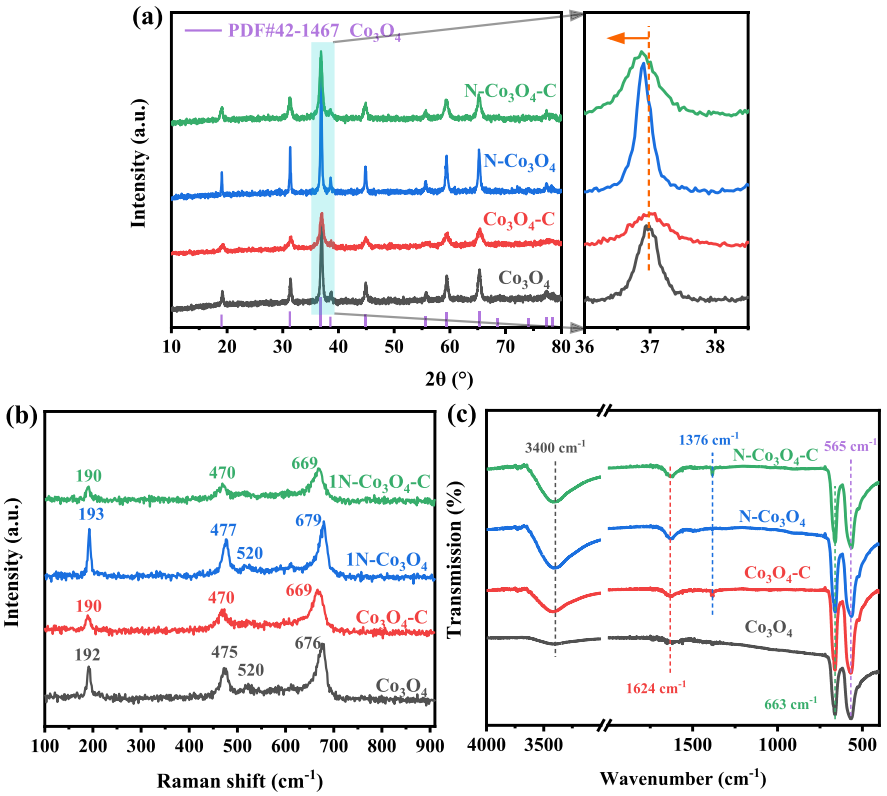

Figure 1. XRD patterns (a), Raman spectra (b), and FT-IR spectra (c) of the Co_3O_4 catalysts.

Co_3O_4.[23] However, the 1-fold Co_3O_4 catalyst still faced inferior catalytic activity in comparison to supported noble metal catalysts. Recently, to improve the catalytic activity of Co_3O_4, many modification strategies, especially doping, have been adopted.[24,25] For example, Ma et al.[26] improved the catalytic performance of Co_3O_4 via indium doping. The results suggested that indium doping distorted the lattice structure and promoted the generation of oxygen vacancies, which enhanced the catalytic activity of Co_3O_4 for gaseous pollutant degradation. Sun et al.[27] found that Cu doping in the (110) facet of Co_3O_4 enhanced its catalytic performance for propane oxidation, which was ascribed to the enhancement of Co−O activation via Cu doping. Except for the metal doping, the nonmetal doping could also boost the catalytic activity of Co_3O_4. For instance, Hu et al.[28] synthesized several N-doped Co_3O_4 catalysts through the g−C_3N_4-modified sol−gel method for N_2O catalytic decomposition. Compared with the pristine Co_3O_4, the N doping in Co_3O_4 promoted the formation of defective structures, basis sites, and surface Co^{2+} on the catalyst and improved the electron donation ability of Co^{2+} and redox properties, which promoted N_2O decomposition. Although the metal or nonmetal doping could greatly improve the catalytic performance of Co_3O_4 for gaseous pollutants degradation, in the actual conditions, the existence of water vapor might suppress VOC adsorption on the catalyst surface and inhibit its degradation. Therefore, the preparation of doping-modified Co_3O_4 and investigation of its catalytic performance for VOC degradation under humid conditions are still indispensable.

Herein, the C, N-codoped N−Co_3O_4−C catalyst was successfully prepared via the solvothermal−calcination method and applied for low-temperature EA catalytic degradation under humid conditions. Compared with Co_3O_4 and C- or N-doped Co_3O_4 catalysts, the C, N-codoped N−Co_3O_4−C catalyst presented excellent catalytic activity (T_{90} = 177 °C) and water resistance (5.0 vol%, T_{90} = 178 °C). Various characterization technologies, including X-ray diffraction (XRD), X-ray absorption spectra (XAS), X-ray photoelectron spectroscopy (XPS), etc., were applied to determine the physical−chemical properties of the catalysts, and the results showed that the C, N codoping weakened the strength of Co−O bonds, increased the surface area, surface Co^{3+}, and O_{ads} species, and improved the low-temperature redox properties and the mobility of lattice oxygen species, which boosted the catalytic performance of N−Co_3O_4−C for EA degradation. Additionally, the weakening of water vapor adsorption on the catalyst surface via N doping to improve the water resistance was uncovered by temperature-programmed H_2O desorption (H_2O-TPD) and theoretical calculations. Namely, the synergistic effect of the C, N codoping enhanced the catalytic activity and water resistance of N−Co_3O_4−C for EA degradation. Meanwhile, the synergistic effect mechanism of C, N codoping was systematically elucidated by in situ diffuse reflectance infrared Fourier transform spectroscopy (DRIFTS) and theoretical calculations. This work provided a new strategy for the preparation of doping-modified catalysts for VOC degradation under humid conditions.

2. EXPERIMENTAL SECTION

2.1. Catalyst Preparation

The doped Co_3O_4 was synthesized by using $CoC_2O_4{\cdot}4H_2O$ as the precursor. The detailed synthesis processes are listed as follows. For N-doped Co_3O_4, first, 2.19 g of $CoC_2O_4{\cdot}4H_2O$ and 0.75 g of urea (molar ratio of Co^{2+} to urea was 1:1) were poured into 100 mL of deionized water and stirred at environmental temperature for 24 h. Furthermore, the mixture suspension liquid was hydrothermal at 100 °C in a breaker for another 24 h. After cooling, the sample was

https://doi.org/10.1021/jacsau.4c01146
JACS Au 2025, 5, 363−380

collected via centrifugation, washed with deionized water, and dried at 80 °C for 12 h. Finally, the collected powder was calcined at 500 °C for 2 h under the heating rate of 5 °C/min in a muffle furnace to obtain N−Co_3O_4. For the N, C-codoped Co_3O_4 catalyst, N−Co_3O_4−C, the synthesis processes were similar to that of N−Co_3O_4, except that the calcination temperature was set at 300 °C. Additionally, 0.5 N−Co_3O_4−C and 2 N−Co_3O_4−C with the Co^{2+}-to-urea molar ratio of 0.5 and 2.0 were also synthesized to investigate the effect of N-doping amount on the catalytic performance. The preparation process was similar to that of N−Co_3O_4−C.

Co_3O_4 and Co_3O_4−C were prepared via the same synthesis processes except that the urea was not added. The detailed information for the preparation of Co_3O_4 and Co_3O_4−C is listed in Supporting Information. The physical and chemical properties of the Co_3O_4 catalysts were measured by many characterization technologies. For detailed information, please refer to Supporting Information.

2.2. Performance Test

EA was chosen as the probe molecule to study the catalytic activity of the as-synthesized catalysts under dry and humid conditions. The detailed processes can be found in Supporting Information.

2.3. Theoretical Calculations

Four model structures with the exposure of the (220) crystal facet of Co_3O_4 and the corresponding C-doped, N-doped, and C, N-codoped samples, namely, Co_3O_4, Co_3O_4−C, N−Co_3O_4, and N−Co_3O_4−C were constructed to calculate the adsorption energies of EA, H_2O, and O_2. Meanwhile, the transition state (TS) searching for the dissociation of EA to ethanol and acetate acid and the dissociation of acetate acid to methanol and formate acid was also calculated. Detailed information about the theoretical calculations is listed in the Supporting Information.

3. RESULTS AND DISCUSSION

3.1. Influence of N-Doping Amount on EA Degradation

First, the influence of the N-doping amount on the EA degradation performance was investigated. All the C, N-codoped Co_3O_4 catalysts with different N-doping amounts displayed the same Fourier transform infrared (FT-IR) spectra (Figure S1), indicating that the N-doping amount presents no influence on the structure of these catalysts. As shown in Figure S2a,b, with the raising of N-doping amount, EA conversions and CO_2 yield enhanced first and then decreased, suggesting that N−Co_3O_4−C presented the optimal EA degradation performance. Therefore, N−Co_3O_4−C with the Co^{2+} and urea molar ratio of 1:1 was selected in the following study.

3.2. Physical Properties and Crystal Structure

The crystal structure of the as-synthesized Co_3O_4 and doped Co_3O_4 was measured by XRD. As depicted in Figure 1a, all of the as-synthesized catalysts exhibited the typical cubic Fd3m spinel structure of Co_3O_4 (PDF#42-4167). Compared with the undoped Co_3O_4, the XRD diffraction peak at a 2θ of ∼37° in N−Co_3O_4 and N−Co_3O_4−C shifted to a lower position, which might be attributed to that N doping induced the substitution of O by the N atom, causing the generation of oxygen vacancies.[29] Additionally, compared with Co_3O_4 and N−Co_3O_4, the diffraction peaks of C-doped catalysts, Co_3O_4−C and N−Co_3O_4−C, were weakened and broadened, which might be attributed to the fact that C doping suppressed the long-range ordering during the crystallization of Co_3O_4.[30] Meanwhile, the crystal size of the samples was calculated via the Scherrer formula according to the diffraction peak of the (311) crystal face in Table S1. Apparently, compared with Co_3O_4 (20.9 nm) and N−Co_3O_4 (25.8 nm), the crystal size of Co_3O_4−C (13.1 nm) and N−Co_3O_4−C (15.1 nm) was smaller, which might be related to the doping of C in the Co_3O_4 lattice. Furthermore, the structure of the as-prepared Co_3O_4 catalysts was investigated via Raman spectra. As shown in Figure 1b, four Raman vibration peaks were found at 192, 477, 520, and 679 cm^{-1}, corresponding to the F_{2g} vibrational band of the tetrahedral CoO_4 site, E_g and F_{2g} vibrational bands of Co_3O_4, and A_{1g} vibrational band of the octahedral CoO_6 site, respectively,[31,32] which further confirmed that the as-prepared catalysts formed a cubic phase. Notably, compared with Co_3O_4, the Raman vibration peaks of the C-doped samples, Co_3O_4−C and N−Co_3O_4−C, shifted to a lower Raman shift (red shift) and became broader, while N−Co_3O_4 presented a positive offset of Raman peaks (blue shift) slightly, which might be related to the change of phonon constraint.[33] Zhong et al.[34] had reported that the red shift of Raman peaks meant the improved phonon constraint and probable lattice distortion or residual stress in nanostructures. Mu et al.[35] reported that the blue shift of Raman bands was ascribed to the confinement influence of photons induced by the formation of oxygen vacancies in the Co_3O_4 surface. Therefore, lattice distortion was formed in Co_3O_4−C and N−Co_3O_4−C, and the oxygen vacancies were generated in the N−Co_3O_4 surface. Additionally, the red shift of Raman shifts in Co_3O_4−C and N−Co_3O_4−C indicated its weakened Co−O bond, which facilitated the mobility of the lattice oxygen species to boost the catalytic activity.[36]

Figure 1c shows the FT-IR spectra of Co_3O_4 and the doped Co_3O_4 catalysts. The vibration bands at 663 and 565 cm^{-1} were assigned to the Co−O vibration of Co^{2+}−O and Co^{3+}−O, respectively,[37,38] which further demonstrated the generation of the cubic Co_3O_4 spinel structure. The vibration bands at 3400 and 1624 cm^{-1} were attributed to the OH group bending vibration and the ν(O−H) mode of physically adsorbed water, respectively.[37] Notably, compared with Co_3O_4 and N−Co_3O_4, a new vibration band at 1376 cm^{-1}, which was ascribed to the characteristic of C−O bond elongation, was observed in Co_3O_4−C and N−Co_3O_4−C, indicating the successful doping of C in the catalyst structure.[39] Therefore, the result of FT-IR spectra suggested the successful transformation of $CoC_2O_4 \cdot 4H_2O$ to Co_3O_4, and the low-temperature calcination caused the doping of C in the structure of Co_3O_4. Meanwhile, the presence of C in Co_3O_4−C and N−Co_3O_4−C could also be confirmed by thermogravimetry (TG) curves and their corresponding derivative thermogravimetry (DTG) curves (Figure S3). The specific surface area and pore size distribution of the samples were measured by physical adsorption apparatus. As shown in Figure S4a, the type-IV isotherm accompanied by an H3 hysteresis loop was observed in all of the catalysts, indicating the presence of mesopores in the catalysts. Furthermore, the pore size distribution (Figure S4b) also confirmed that the as-synthesized catalysts were mesoporous materials. Table S1 summarizes the surface area and total pore volume of these Co_3O_4 catalysts. Compared with Co_3O_4 (32.5 m^2/g and 0.262 cm^3/g) and N−Co_3O_4 (23.6 m^2/g and 0.115 cm^3/g), a higher specific surface area was observed in Co_3O_4−C (123 m^2/g and 0.369 cm^3/g) and N−Co_3O_4−C (76 m^2/g and 0.277 cm^3/g), which might be ascribed to the doping of C in the catalysts. The higher surface area could improve the adsorption and mass transfer of the VOC molecules to accelerate their degradation.

Scanning electron microscopy (SEM) images and their corresponding element mapping were carried out to study the morphology and element distributions of N−Co_3O_4−C. As

https://doi.org/10.1021/jacsau.4c01146
JACS Au 2025, 5, 363−380

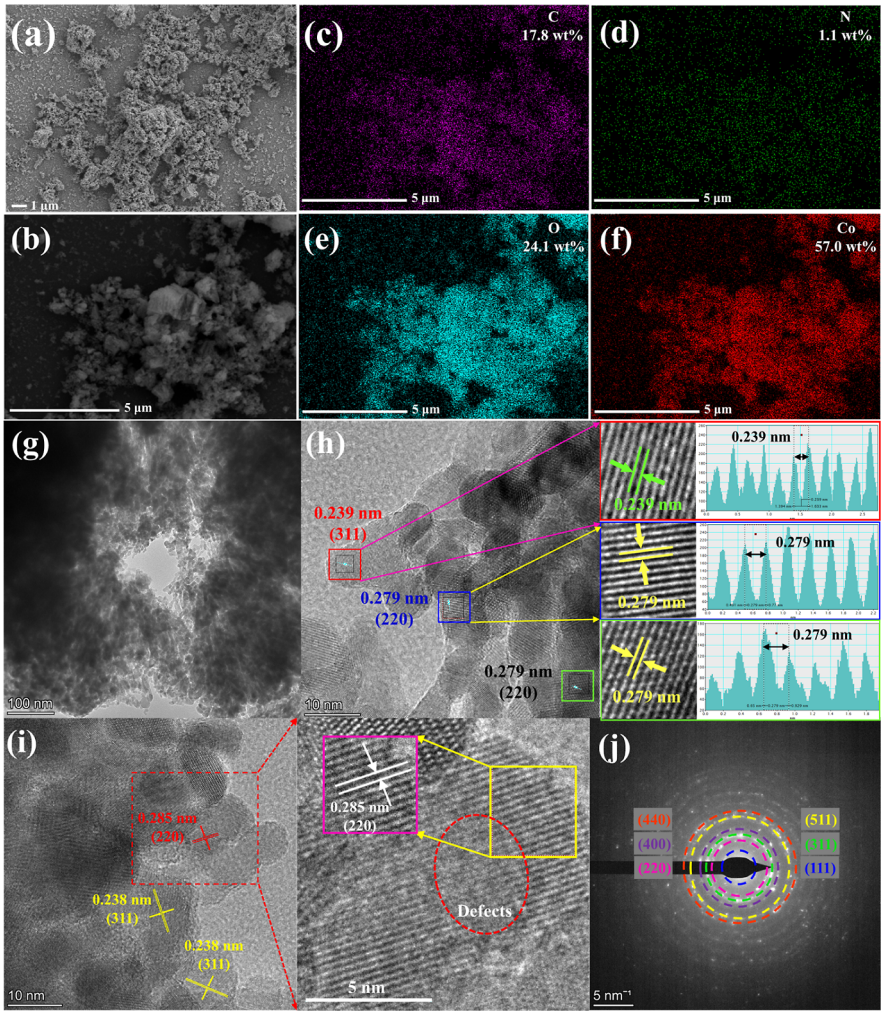

Figure 2. SEM images and corresponding element mapping (a–f), TEM images (g), HRTEM (h,i) images, and SAED pattern (j) of N–Co_3O_4–C.

presented in Figure 2a–f, the SEM images showed an irregular shape. Meanwhile, the Co and O elements were evenly dispersed on the catalyst surface. In addition to the presence of Co and O, the existence of C and N elements was also observed, indicating the successful doping of C and N in N–Co_3O_4–C. Furthermore, transmission electron microscopy (TEM) and high-resolution TEM (HRTEM) images were also used to investigate the textural structure of the N–Co_3O_4–C catalysts. As presented in Figures S5 and 2g, N–Co_3O_4–C presented an irregular circle shape with an average particle size of 11.85 nm. Figure 2h,i displays the HRTEM images and the enlarged lattice fringes of N–Co_3O_4–C. As depicted in Figure 2h, the lattice spaces of 0.239 and 0.279 nm, corresponding to the (311) and (220) lattice faces of Co_3O_4, were observed. Meanwhile, similar exposed crystal faces are also found in Figure 2i. However, compared with Figure 2h, the wider lattice space of the (220) crystal face was found in the enlarged images of Figure 2i, and obvious lattice distortion was also observed. The enlarged lattice space might be ascribed to the N replaced with O in N–Co_3O_4–C. Meanwhile, because the radius of the N atom is larger than that of the O atom, this substitution would induce the expansion of lattice space, leading to the low angle shift of the Bragg diffraction angle and the formation of oxygen vacancies. This result was consistent with the results of the XRD patterns (Figure 1a). The formation of lattice distortion might be ascribed to the C doping. Furthermore, the selected area electron diffraction (SAED) pattern (Figure 2j) also presented the (111), (220), (311), (400), (511), and (440) crystal planes of Co_3O_4, which suggested the good crystallinity characteristics of Co_3O_4. Additionally, TEM, HRTEM, and SAED patterns were also applied to investigate the crystal structure of Co_3O_4 (Figures S6 and S7), Co_3O_4–C (Figures S8 and S9), and N–CO_3O_4 (Figures S10 and S11). The average particle sizes of Co_3O_4, Co_3O_4–C, and N–Co_3O_4 were 21.86, 8.37, and 23.16 nm, respectively, which was consistent with the XRD result (Table S1). Meanwhile, C doping caused the lattice distortion, and N doping induced the oxygen vacancies, which were also confirmed by these HRTEM images of the as-prepared Co_3O_4 catalysts.

3.3. Surface Chemical Composition and Redox Properties

Figure 3a–d displays the C 1s, Co 2p, and N 1s XPS spectra of the catalysts, respectively. As shown in Figure 3a, for Co_3O_4 and N–Co_3O_4, the C 1s spectra were fitted into C–C, C–O, and C=O bonds at 284.8, 286.6, and 288.8 eV, respectively.[40,41] After the doping of C in Co_3O_4–C and N–Co_3O_4–C, a new peak at 289.1 eV, corresponding to the C–Co–O bond, was observed, which indicated the successful doping of C in Co_3O_4–C and N–Co_3O_4–C.[42,43] For the Co 2p orbit (Figure 3b), two evident peaks at 780.3 and 795.4 eV, attributed to the Co $2p_{3/2}$ and Co $2p_{1/2}$ orbits, were found. Co

https://doi.org/10.1021/jacsau.4c01146
JACS Au 2025, 5, 363–380

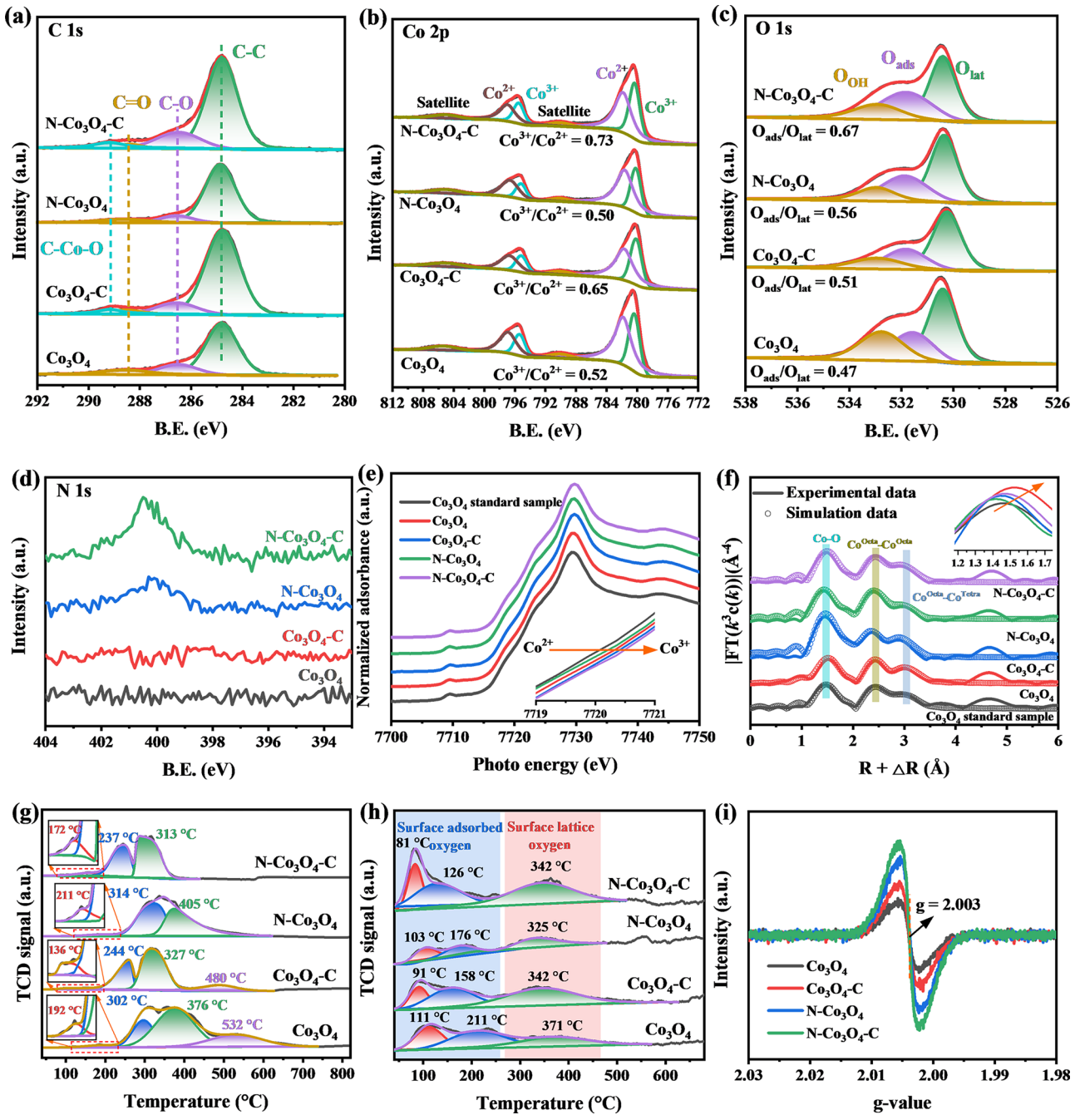

Figure 3. C 1s (a), Co 2p (b), O 1s (c), and N 1s (d) XPS spectra; normalized Co K-edge XANES spectra (e); Co K-edge EXAFS $k^3\chi(R)$ (f); H_2-TPR profiles (g); O_2-TPD profiles (h); and ESR spectra (i) of the Co_3O_4 catalyst.

$2p_{3/2}$ spectra were deconvoluted into the Co^{3+} in octahedral coordination and Co^{2+} in tetrahedral coordination, attended with a satellite peak at 780.3, 781.8, and 790.0 eV, respectively. For the Co $2p_{1/2}$ orbit, three peaks located at 795.3 eV (Co^{3+}), 796.8 eV (Co^{2+}), and 805.2 eV (satellite peak) were also observed.[11,44] The molar ratio of Co^{3+}/Co^{2+} was calculated based on the peak areas (Table S1). As illustrated in Table S1, the surface Co^{3+}/Co^{2+} molar ratio followed the order N−Co_3O_4−C (0.73) > Co_3O_4−C (0.65) > Co_3O_4 (0.52) > N−Co_3O_4 (0.50). Apparently, N−Co_3O_4−C presented the largest surface Co^{3+} species. The O 1s spectra of the Co_3O_4 catalysts are displayed in Figure 3c. The O 1s orbits were deconvoluted into lattice oxygen (O_{lat}), surface-adsorbed oxygen (O_{ads}) species, and surface hydroxy from adsorbed H_2O (O_{OH}) at 530.3, 531.6, and 532.9 eV, respectively.[4,17] Generally, surface O_{ads} species originated from the gaseous oxygen species adsorbed on the surface oxygen vacancies, which were positively correlated with the oxygen vacancy concentrations.[1] Therefore, the surface O_{ads}/O_{lat} molar ratios of as-prepared Co_3O_4 were calculated (Table S1). The surface O_{ads}/O_{lat} molar ratios of the Co_3O_4 catalysts were abided by the following order: N−Co_3O_4−C (0.67) > N−Co_3O_4 (0.56) > Co_3O_4−C (0.51) > Co_3O_4 (0.47), which indicated that the doping of N in N−Co_3O_4−C and N−Co_3O_4 induced the formation of more oxygen vacancies. To further confirm the successful doping of N in N−Co_3O_4−C and N−Co_3O_4, the N 1s XPS spectra were collected. As shown in Figure 3d, compared with Co_3O_4 and Co_3O_4−C, a distinct peak was found in the N 1s

https://doi.org/10.1021/jacsau.4c01146
JACS Au 2025, 5, 363−380

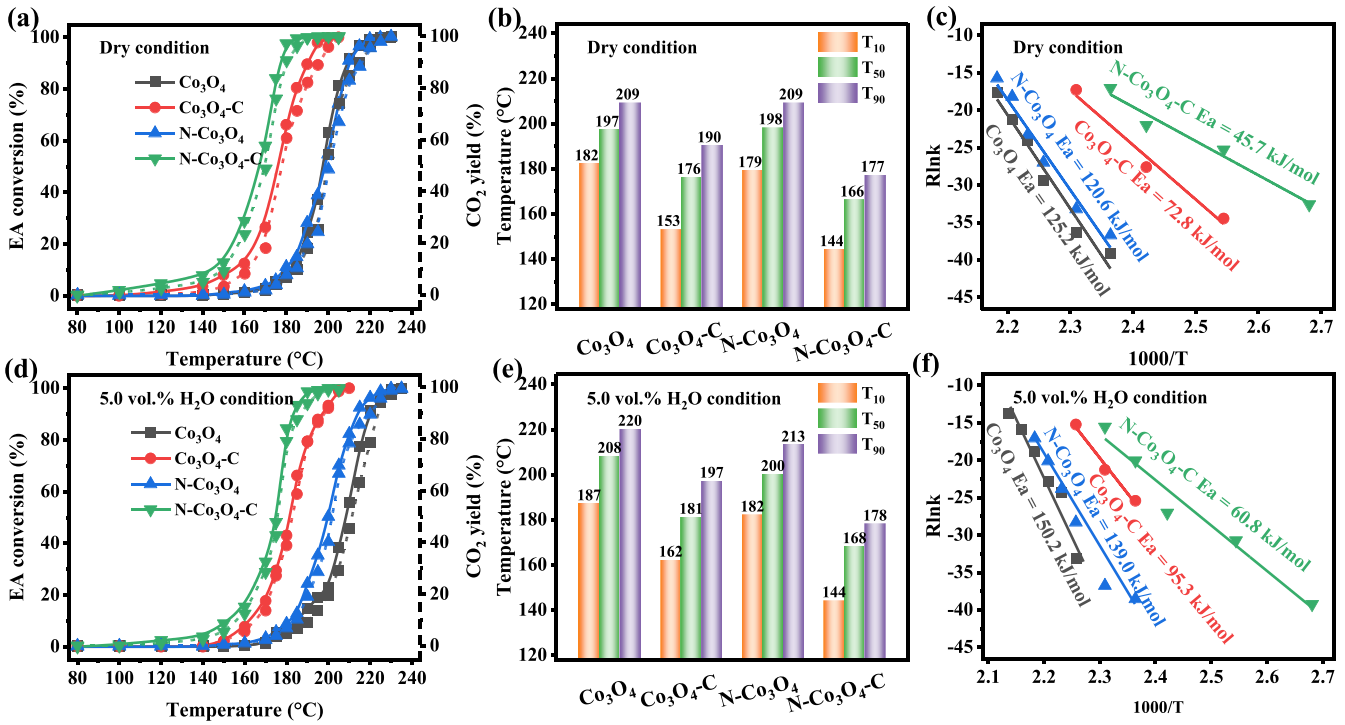

Figure 4. EA conversion and CO_2 yield (a,d); values of T_{10}, T_{50}, and T_{90} (b,e); and Ea plots (c,f) over the Co_3O_4 catalysts under dry (a−c) and humid (d−f) conditions.

XPS spectra of N−Co_3O_4−C and N−Co_3O_4, further suggesting the successful doping of N.

Furthermore, the local atomic coordination environment of the Co_3O_4 catalysts was investigated by XAS. As depicted in Figure 3e, the X-ray absorption near-edge structure (XANES) spectra of the as-prepared Co_3O_4 catalysts displayed a similar absorption edge with the Co_3O_4 standard sample, indicating all the as-prepared Co_3O_4 catalysts presented the near-identical oxidation state of Co. However, the position of the absorption edge (the purple arrow in the enlarged pattern of Figure 3e) exhibited different oscillations. Compared with Co_3O_4, the Co K-edge spectra of the C-doped and C, N-codoped Co_3O_4 shifted to higher energy, while the Co K-edge spectrum of N-doped Co_3O_4 slightly shifted to lower energy, suggesting that the average oxidation states of Co in the as-synthesized Co_3O_4 followed N−Co_3O_4−C > Co_3O_4−C > Co_3O_4 > N−Co_3O_4. Namely, N−Co_3O_4−C possessed the richest Co^{3+} species, followed by Co_3O_4−C, Co_3O_4, and N−Co_3O_4, which was in accord with the results of Co 2p XPS spectra. The extended X-ray absorption fine structure (EXAFS) spectra of Co K-edge and Fourier transforms for k^3-weighted Co K-edge EXAFS spectra were fitted (Figures 3f and S12). Meanwhile, the wavelet transforms of the samples were provided (Figure S13). The EXAFS fitting parameters are summarized in Table S2. As shown in Figure 3f, the peaks at ∼1.5, 2.4, and 3.0 Å were ascribed to the single scattering paths of Co to the closest neighboring O, namely, the Co−O coordination, the Co−Co coordination of the adjacent octahedral Co^{3+} site (Co^{Octa}−Co^{Octa}), and the Co−Co coordination of the nearby tetrahedral Co^{2+} site and octahedral Co^{3+} site (Co^{Tetra}−Co^{Octa}), respectively.[45] It had been reported that the Co−O peak in the EXAFS spectra shifted to a higher R-value, indicating the weakening of the Co−O bond.[46] Herein, as depicted in the enlarged pattern in Figure 3f, compared with Co_3O_4 and N−Co_3O_4, the *R*-value of Co_3O_4−C and N−Co_3O_4−C shifted to a higher *R*-value, suggesting the weakening of the Co−O bond in Co_3O_4−C and N−Co_3O_4−C, which was consistent with the Raman results (Figure 1b). Additionally, compared with the Co_3O_4 standard sample (1.92 Å), the Co−O bond distance in Co_3O_4−C (1.95 Å) and N−Co_3O_4−C (1.96 Å) was enhanced, which also confirmed the weakening of the Co−O bond via C doping. Therefore, the weakening of the Co−O bond in the Co_3O_4−C and N−Co_3O_4−C catalysts was attributed to the doping of C.

Figure 3g displays the temperature-programmed H_2 reduction (H_2-TPR) profiles of the Co_3O_4 catalysts. Meanwhile, the H_2 consumption was calculated according to the peak area (Table S3). As depicted in Figure 3g, the small reduction peak in the enlarged pattern (inset in Figure 3g) was ascribed to the reduction of surface oxygen species.[47] The other peaks were attributed to the reduction of the lattice oxygen species. For the undoped Co_3O_4, the reduction peak at 302 °C was assigned to the reduction of Co_3O_4 to CoO.[48] The other two reduction peaks at 376 and 532 °C were attributed to the gradual reduction of CoO to Co.[49] After the doping of C in Co_3O_4−C and N−Co_3O_4−C, the reduction temperature shifted to a lower temperature, suggesting the enhancement of the redox properties via C doping. However, the doping of N in N−Co_3O_4 did not improve its redox properties. Although the calculated H_2 consumption (Table S3) was not consistent with the reduction temperature, the great decrease in the reduction temperature in Co_3O_4−C and N−Co_3O_4−C could demonstrate their better low-temperature reducibility. Thus, the reduction ability of the as-prepared Co_3O_4 catalysts obeyed the following order: N−Co_3O_4−C > Co_3O_4−C > Co_3O_4 > N−Co_3O_4, indicating that N−Co_3O_4−C exhibited the optimal low-temperature redox properties. Meanwhile, the doping of C could greatly enhance the reducibility of the catalysts at a low temperature.

https://doi.org/10.1021/jacsau.4c01146
JACS Au 2025, 5, 363−380

As presented in Figure 3h, the temperature-programmed O_2 desorption (O_2-TPD) profiles of the Co_3O_4 catalysts were fitted and identified as three regions at below 300 °C, 300−500 °C, and above 500 °C, which were ascribed to the surface-adsorbed oxygen species, surface lattice oxygen species, and bulk lattice oxygen species, respectively.[18] Generally, the surface-adsorbed oxygen species, as the main active oxygen species, played a significant role in an oxidation reaction.[46] Meanwhile, the lower release temperature of surface-adsorbed oxygen species indicated its better mobility. The release temperature of surface-adsorbed oxygen species in the as-synthesized Co_3O_4 catalysts followed N−Co_3O_4−C < Co_3O_4−C < N−Co_3O_4 < Co_3O_4, suggesting that N−Co_3O_4−C presented the best mobility of surface-adsorbed oxygen species. Furthermore, the oxygen desorption amount was calculated according to the fitted peak area (Table S4). Compared with other Co_3O_4 catalysts, the biggest surface-adsorbed oxygen species (0.051 mmol/g) was observed in N−Co_3O_4−C, indicating its highest surface-adsorbed oxygen species capacity. Additionally, the largest desorption amount (0.036 mmol/g) of surface lattice oxygen species was also observed in N−Co_3O_4−C, suggesting its superior surface lattice oxygen capacity ability. According to the above analysis, the improvement of surface-adsorbed oxygen mobility and surface oxygen capacity was found in the N−Co_3O_4−C catalyst.

As mentioned in the XRD patterns, HRTEM images, and O 1s XPS spectra, the doping of N in Co_3O_4 induced the generation of oxygen vacancies. To confirm the production of oxygen vacancies directly, electron spin resonance (ESR) was carried out. As shown in Figure 3i, the peak at g = 2.003, which presented the capture of unpaired electrons by oxygen vacancies, was observed in all of the Co_3O_4 catalysts. Compared with Co_3O_4 and Co_3O_4−C, the N-doped samples presented a stronger ESR signal, suggesting the successful introduction of oxygen vacancies via N doping, which was consistent with the XRD, HRTEM, and O 1s XPS results.

3.4. EA Degradation Performance, Stability, and Water Resistance

The catalytic activity of the as-synthesized Co_3O_4 catalysts was determined via EA degradation under dry and humid (5.0 vol% H_2O) conditions. Figure 4a presents EA conversion and CO_2 yield for EA degradation over the as-prepared catalysts. As shown in Figure 4a, the EA conversion and the corresponding CO_2 yield over Co_3O_4 and N−Co_3O_4 were similar, suggesting that the doping of N did not improve the catalytic performance. However, compared with Co_3O_4, the EA degradation activity and the corresponding CO_2 yield over C-doped Co_3O_4 and C, N-codoped Co_3O_4 were greatly enhanced. Meanwhile, the temperatures of EA conversion at 10, 50, and 90% (T_{10}, T_{50}, and T_{90}) were also calculated to further estimate the catalytic performance of the Co_3O_4 catalysts, and the results are listed in Figure 4b and Table S5. The T_{50} and T_{90} values of Co_3O_4, Co_3O_4−C, N−Co_3O_4, and N−Co_3O_4−C were 197 and 209 °C, 176 and 190 °C, 198 and 209 °C, and 166 and 177 °C, respectively, which further confirmed that the C doping improved EA degradation. Additionally, compared with the commercial Co_3O_4 for EA degradation (Figure S14), the as-prepared Co_3O_4 catalysts displayed a better catalytic performance for EA oxidation. Meanwhile, compared with the reported metal oxide catalysts, even supported noble metal catalysts listed in Table S6, the N−Co_3O_4−C catalysts also presented excellent catalytic performance. Additionally, the active energy (Ea, Figure 4c), reaction rate (r, Figure S15a), and the reaction rate normalized by the surface area (r_s, Figure S15b) were also calculated. The Ea values of Co_3O_4, Co_3O_4−C, N−Co_3O_4, and N−Co_3O_4−C were 125.2, 72.8, 120.6, and 45.7 kJ/mol, respectively, suggesting that the C, N-codoped N−Co_3O_4−C presented the best EA degradation activity. However, r and r_s displayed an inverse result. N−Co_3O_4−C and Co_3O_4−C presented a higher r than that of Co_3O_4 and N−Co_3O_4, while r_s was low, which suggested that the higher surface area induced by C doping was the main reason for the great performance of N−Co_3O_4−C and Co_3O_4−C for EA degradation. The characterization results suggested that the C doping weakened the Co−O bond strength (Figures 1b and 3f) and greatly improved the redox properties (Figure 3g) and surface chemical adsorbed oxygen amount (Figure 3h). Meanwhile, the high surface area could enhance the VOCs' adsorption capacity. Therefore, the role of C doping was the enhancement of the surface area, redox properties, and surface chemical adsorbed oxygen amount, which induced the improvement of catalytic performance. Besides, the turnover frequency based on Co (TOF_{Co}) of the as-prepared Co_3O_4 catalysts was calculated at 150 °C (Table S5). N−Co_3O_4−C presented the highest TOF_{Co} value (4.22×10^{-4} s^{-1}), followed by Co_3O_4−C (2.67×10^{-4} s^{-1}), Co_3O_4 (0.34×10^{-4} s^{-1}), and N−Co_3O_4 (0.31×10^{-4} s^{-1}).

Figure 4d,e presents the EA conversion, the corresponding CO_2 yield, and the T_{10}, T_{50}, and T_{90} values of EA oxidation over the Co_3O_4 catalysts under humid conditions (5.0 vol% H_2O). Compared with the dry conditions, the EA conversion, corresponding CO_2 yield, r (Figure S15c), and r_s (Figure S15d) were decreased at the same temperature. Meanwhile, the Ea values (Figure 4f) were increased, suggesting that the addition of water vapor in the reaction system inhibited EA degradation over the Co_3O_4 catalysts. T_{50} and T_{90} values of Co_3O_4, Co_3O_4−C, N−Co_3O_4, and N−Co_3O_4−C were 208 and 220 °C, 181 and 197 °C, 200 and 213 °C, and 168 and 178 °C, respectively. Apparently, the N-doped samples presented better water resistance, which could be further confirmed by the r and r_s in Figure S15. Therefore, it could be inferred that the N-doping-induced oxygen vacancies were related to the water resistance of the catalysts, which will be further discussed in the following.

In general, the catalytic activity of a catalyst was determined by its physical chemical properties. According to the above characterization results, it could be concluded that although the doping of N in Co_3O_4 led to the generation of oxygen vacancies, the reducibility was weakened (Figure 3g), and the Co−O bond intensity was enhanced (Figures 1b and 3f), which caused its poor EA degradation performance in comparison to Co_3O_4. The C doping weakened the strength of the Co−O bond, which enhanced the low-temperature redox properties and the activation of surface lattice oxygen species. Meanwhile, the doping of C in Co_3O_4 improved the specific surface area greatly, which could boost the adsorption of EA and promote its degradation. Furthermore, it had been reported that the higher content of Co^{3+} ions on the catalyst surface probably played a role in the improved catalytic activity for VOC degradation.[19] Therefore, the optimal catalytic activity of N−Co_3O_4−C might be due to its high surface oxygen vacancies induced by N doping, the C-doping-caused weak Co−O bond, large surface area and low-temperature reducibility, and the largest surface Co^{3+} species.

https://doi.org/10.1021/jacsau.4c01146
JACS Au 2025, 5, 363−380

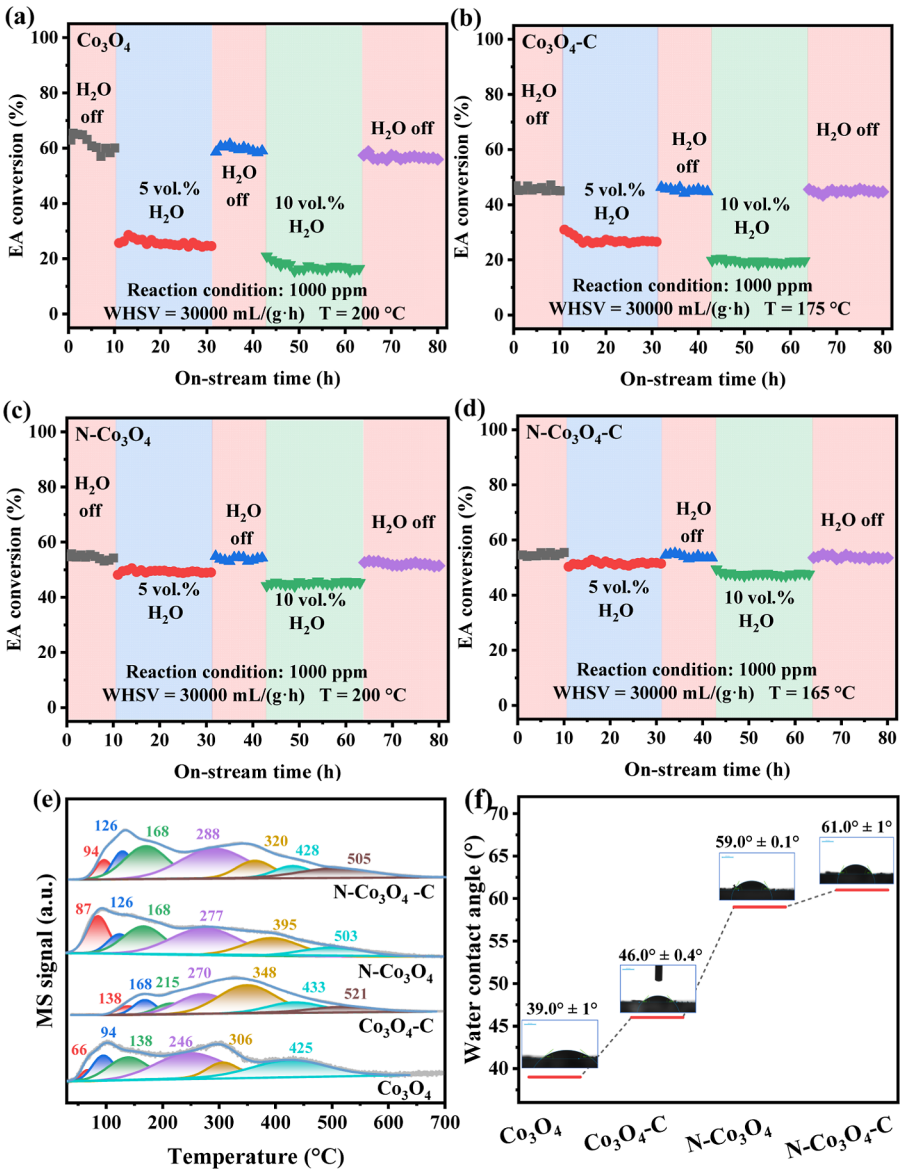

Figure 5. Water-resistance test of the Co_3O_4 catalysts for EA oxidation (a–d), H_2O-TPD (e), and water contact angle (f) of the Co_3O_4 catalysts (the H_2O-TPD profiles of Co_3O_4 and N–Co_3O_4 were enlarged 5 times).

Additionally, N–Co_3O_4–C with the optimal EA degradation performance was selected to investigate the effect of weight hourly space velocity (WHSV) and the reusability. As shown in Figure S16, with the improvement of WHSV from 30,000 to 120,000 mL/(gh), EA conversion and the corresponding CO_2 yield decreased, which suggested that the catalytic performance of N–Co_3O_4–C was influenced by the WHSV. Figure S17 presents the reusability of N–Co_3O_4–C for EA degradation. After being reused five times, the catalytic activity of N–Co_3O_4–C was decreased slightly. To investigate the reason, the XPS spectra of N–Co_3O_4–C after five times reuse were investigated. As shown in Figure S18, compared with the fresh N–Co_3O_4–C, after several times being reused, the surface Co^{3+} and O_{ads} species were decreased, which might be the reason that caused the decrease of catalytic performance.

Catalytic stability and water resistance were important targets of the catalysts for practical application. Therefore, the catalytic stability and water resistance of the Co_3O_4 catalysts were tested. As shown in Figure S19, all of the Co_3O_4 catalysts presented great stability for EA oxidation. Meanwhile, the XRD patterns (Figure S20a), Raman spectra (Figure S20b), and the FT-IR spectra (Figure S20c) also confirmed the great stability of the Co_3O_4 catalysts. Figure 5a–d presents the water-resistance test of Co_3O_4, Co_3O_4–C, N–Co_3O_4, and N–Co_3O_4–C for EA degradation at different temperatures, respectively. As depicted in Figure 5a–d, the introduction of 5.0 vol% water vapor into the reaction system caused the decreased EA conversion over these Co_3O_4 catalysts, especially for Co_3O_4 and Co_3O_4–C, which suggested the inhibition of water vapor on EA degradation, which was consistent with the results of Figure 4d. When the increase of water vapor to 10.0 vol%, EA conversion only slightly decreased. Furthermore, EA conversion could be regained to the initial after the water vapor was cut off, which might be ascribed to the easy desorption of water vapor from the catalyst surface at high temperature.[46] However, compared with Co_3O_4 and Co_3O_4–C, the water vapor exhibited a smaller influence on EA

https://doi.org/10.1021/jacsau.4c01146
JACS Au 2025, 5, 363–380

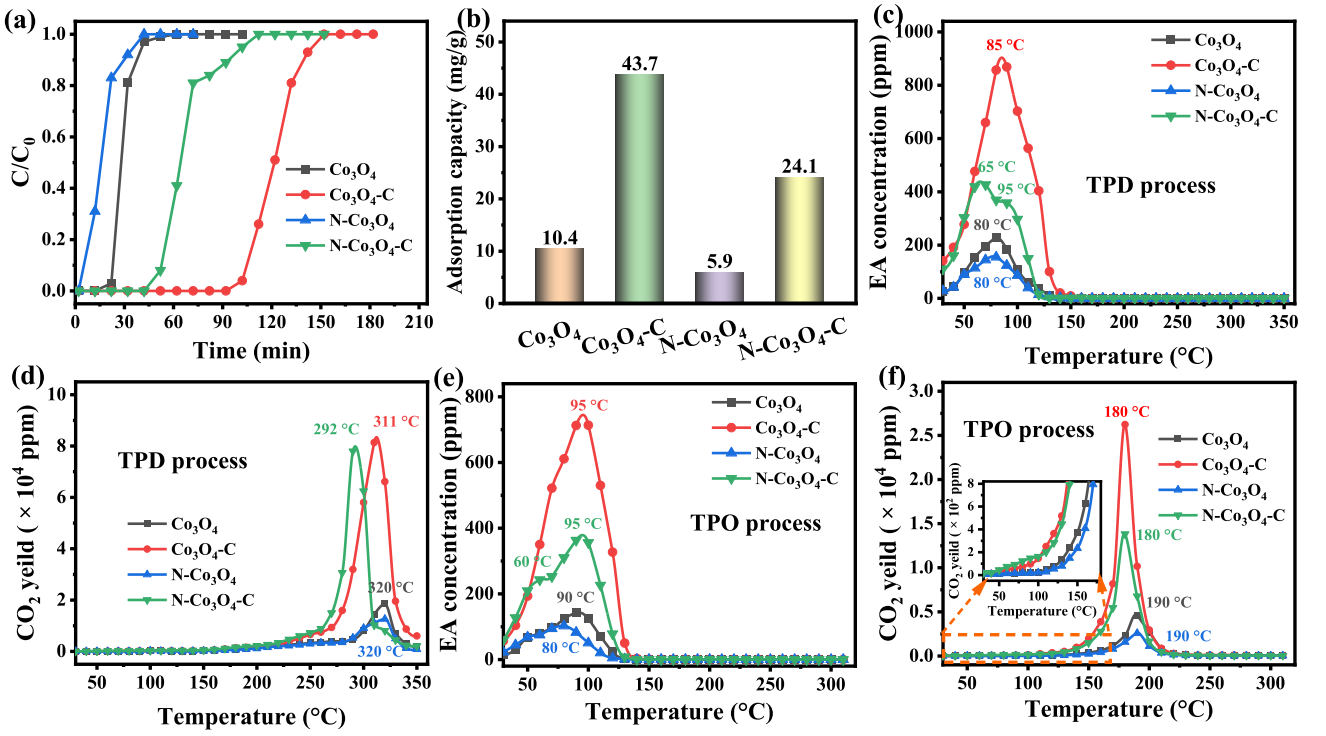

Figure 6. Breakthrough curve (a) of the Co_3O_4 catalysts for EA and the corresponding adsorption capacity (b); EA−TPD and EA−TPO profiles of the Co_3O_4 catalysts: (c,e) EA concentration and (d,f) CO_2 generation.

conversion over the N-doped samples (Figure 5c,d), indicating the better water resistance of the N-doped catalysts.

To investigate the reason for the great water resistance of the N-doped Co_3O_4, N−Co_3O_4, and N−Co_3O_4−C, the H_2O-TPD and water contact angle (H_2O−CA) of the as-prepared Co_3O_4 catalysts were investigated. As shown in Figure 5e, compared with Co_3O_4 and N−Co_3O_4, Co_3O_4−C and N−Co_3O_4−C presented stronger H_2O-TPD peaks, which might be related to the surface area. Additionally, the H_2O-TPD profiles of the as-prepared Co_3O_4 catalysts were fitted into several peaks. Generally, the desorbed water vapor in H_2O-TPD was divided into three regions at temperatures below 150 °C, 150−300 °C, and above 300 °C, corresponding to the physically adsorbed water species (Type I), associative adsorbed water species (Type II), and dehydration of hydroxide species (Type III).[50] According to the literature,[51,52] the interaction between water vapor and surface-active oxygen species could induce the formation of a surface hydroxyl group, which might participate in the oxidation of VOCs. Meanwhile, because of its ability to provide active protons, the associatively adsorbed water species might be the active site for VOC oxidation.[52] Table S7 summarizes the content of different types of adsorbed H_2O on the catalysts. Compared with Co_3O_4 (34.55%) and Co_3O_4−C (38.96%), the content of associatively adsorbed water species (Type II) in the N-doped samples, N−Co_3O_4 (51.03%) and N−Co_3O_4−C (56.82%), increased greatly. It had been reported that the associatively adsorbed water species were formed in the oxygen vacancies in the sample, which was likely to be the active oxygen species for VOC oxidation.[50,53] Therefore, the N-doping-induced oxygen vacancies in N−Co_3O_4 and N−Co_3O_4−C could interact with water vapor to generate the associatively adsorbed water species, providing active oxygen species and enhancing their water resistance. Figure 5f displays the CA of the as-prepared Co_3O_4 catalysts. Obviously, the hydrophobic angles of N−Co_3O_4−C (61.0 ± 1°) and N−Co_3O_4 (59.0 ± 0.1°) were increased after N doping in comparison to Co_3O_4 (39.0 ± 1°) and Co_3O_4−C (46.0 ± 0.4°). Gao et al.[54] reported that the decoration of N in MIL-125(Ti) enhanced the hydrophobicity of the catalytic surface to boost the water resistance for CH_3CHO degradation. Herein, the same phenomenon was also observed. Therefore, according to the above analysis, the N doping induced the formation of oxygen vacancies, and the improvement of the hydrophobic angle might be the reason for the better water resistance of N−Co_3O_4 and N−Co_3O_4−C for EA oxidation.

3.5. Adsorption and Activation of EA

To better learn the adsorption−desorption and activation of EA on the Co_3O_4 catalysts and the role of lattice and gaseous oxygen species in EA oxidation, EA adsorption breakthrough curves were obtained, and EA temperature-programmed desorption and oxidation (EA−TPD and EA−TPO) were performed. As shown in Figure 6a, the EA adsorption breakthrough time of the as-prepared Co_3O_4 catalysts followed the order Co_3O_4−C > N−Co_3O_4−C > Co_3O_4 > N−Co_3O_4. Meanwhile, the adsorption capacity of these catalysts for EA adsorption was also calculated according to the breakthrough curves based on the formulas in our previous work.[13] As depicted in Figure 6b, Co_3O_4−C presented the highest EA adsorption capacity (43.7 mg/g), followed by N−Co_3O_4−C (24.1 mg/g), Co_3O_4 (10.4 mg/g), and N−Co_3O_4 (5.9 mg/g). Apparently, compared with Co_3O_4 and N−Co_3O_4, the C-doped samples, Co_3O_4−C and N−Co_3O_4−C, exhibited higher EA adsorption capacity, which was ascribed to their high surface area induced by C doping. Therefore, it could be concluded that the doping of C in Co_3O_4−C and N−Co_3O_4−C could improve the EA adsorption performance.

https://doi.org/10.1021/jacsau.4c01146
JACS Au 2025, 5, 363−380

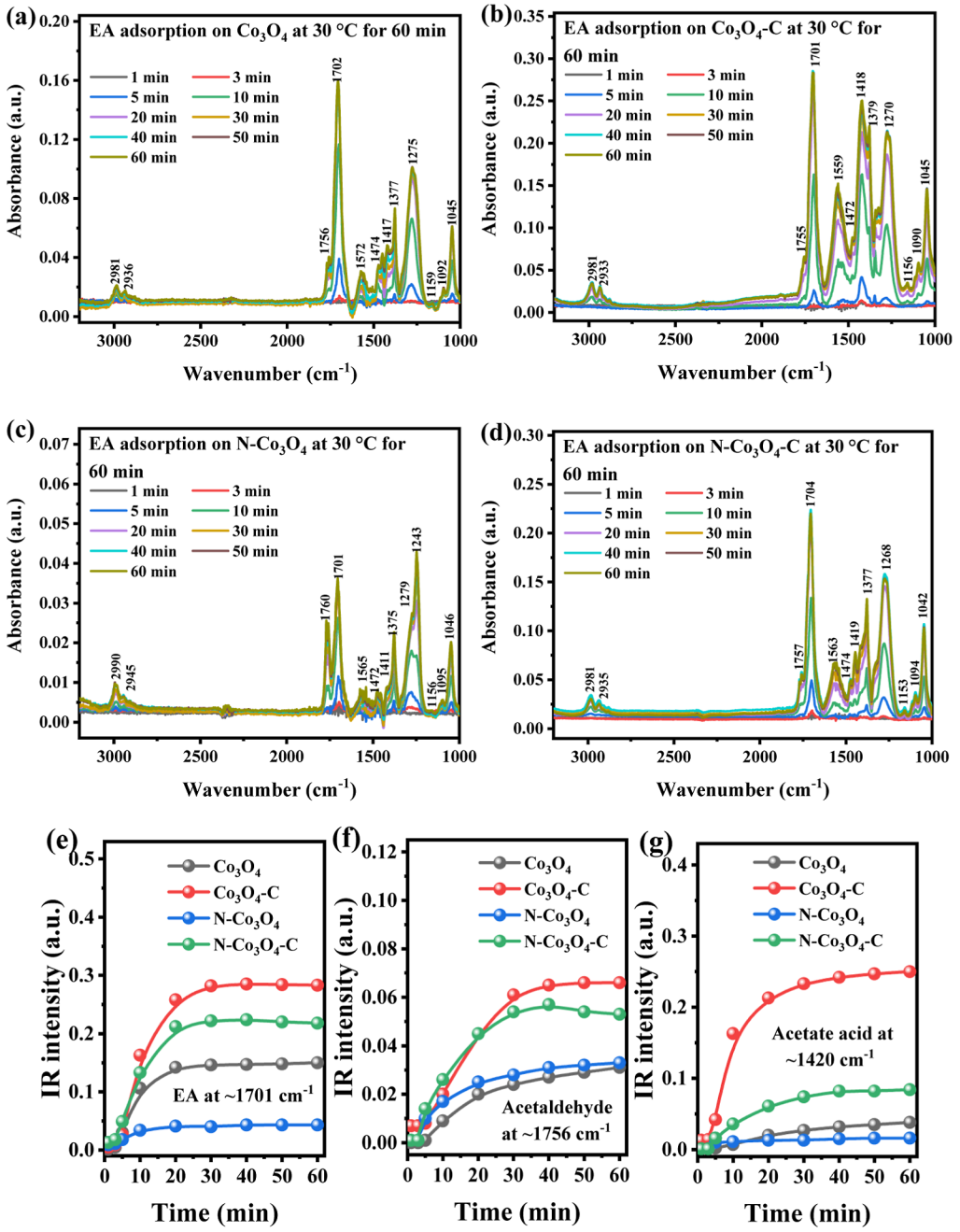

Figure 7. In situ DRIFTS spectra for EA adsorption over Co_3O_4 (a), Co_3O_4−C (b), N−Co_3O_4 (c), and N−Co_3O_4−C (d) and the plots of IR signal intensities of the surface-adsorbed EA (e), acetaldehyde (f), and acetate acid (g) over the as-prepared Co_3O_4 catalysts.

Furthermore, the EA desorption behavior over the as-prepared Co_3O_4 catalysts was investigated by EA−TPD after adsorption saturation. Figure 6c,d displays the EA concentration and CO_2 yield during the TPD process. As presented in Figure 6c, the EA desorption peaks over Co_3O_4, Co_3O_4−C, N−Co_3O_4, and N−Co_3O_4−C were centered at 80, 85, 80, and 95 °C, respectively, which indicated that the C-doped samples, Co_3O_4−C and N−Co_3O_4−C, exhibited stronger EA adsorption ability. Meanwhile, the EA desorption peak area also confirmed the higher EA adsorption capacity of the C-doped samples. Figure 6d depicts the generation of CO_2 during the TPD process. The generation of CO_2 was attributed to the reaction between adsorbed EA and lattice oxygen species. As shown in Figure 6d, the initial CO_2 generation temperature over the as-prepared Co_3O_4 catalysts followed the order of N−Co_3O_4−C < Co_3O_4−C < Co_3O_4 < Co_3O_4−N. Furthermore, the generation of CO_2 over Co_3O_4, Co_3O_4−C, N−Co_3O_4, and N−Co_3O_4−C were centered at 320, 311, 320, and 292 °C, respectively. This result suggested easier activation of the Co−O bond in the C-doped samples, which was in accord with the results of Raman spectra (Figure 1b) and EXAFS spectra (Figure 3f). Additionally, the adsorption-saturated samples were subjected to the TPO process under 5.0 vol% O_2 balanced with an Ar atmosphere to investigate the gaseous oxygen activation ability of the as-prepared Co_3O_4 catalysts. As presented in Figure 6e, compared with the TPD process (Figure 6c), the desorbed EA concentration in the TPO process decreased greatly, indicating that the introduction of

https://doi.org/10.1021/jacsau.4c01146
JACS Au 2025, 5, 363−380

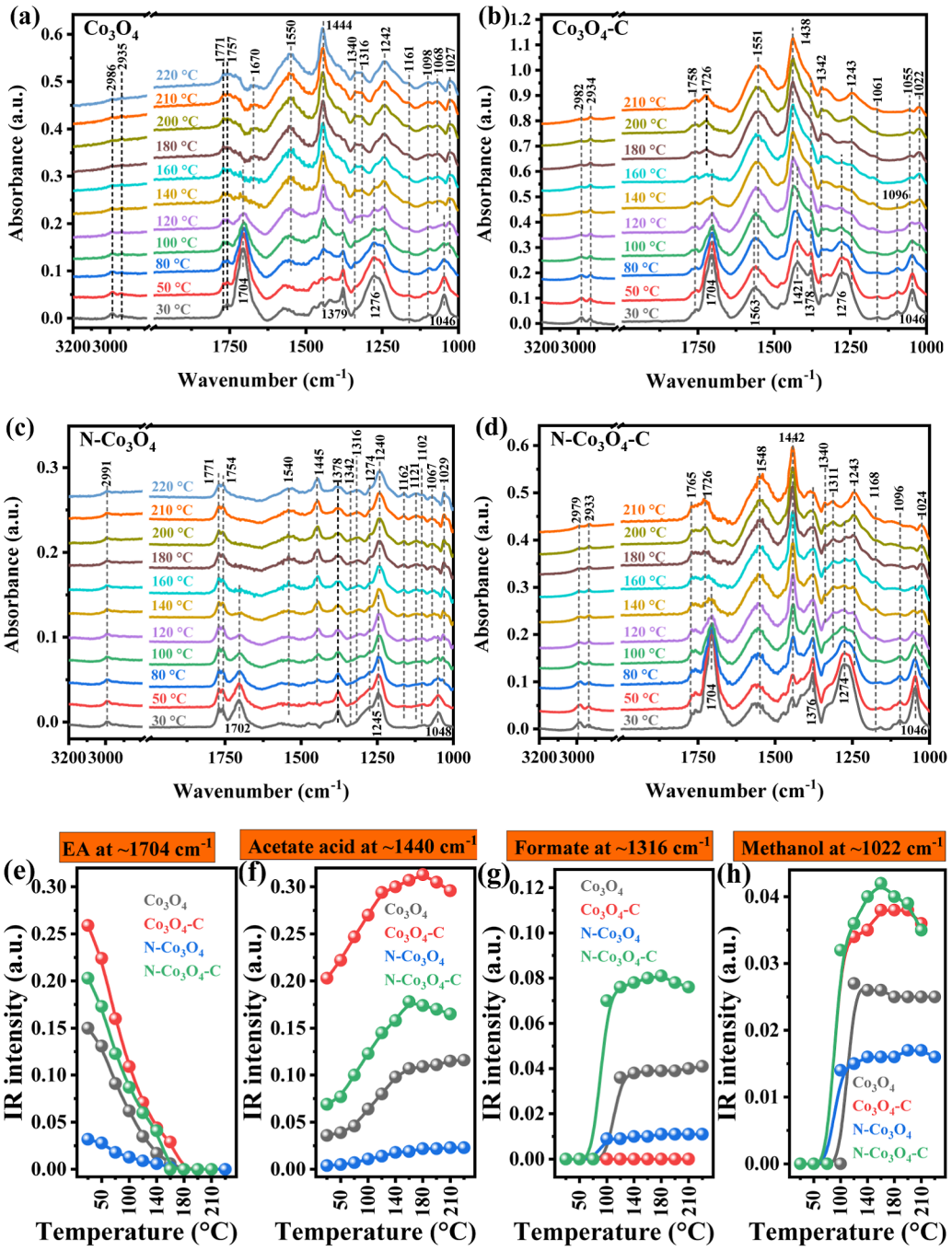

Figure 8. In situ DRIFTS spectra for EA oxidation at different temperatures over Co_3O_4 (a), Co_3O_4−C (b), N−Co_3O_4 (c), and N−Co_3O_4−C (d) and the plots of IR signal intensities of the surface-adsorbed EA (e), acetate acid (f), formate (g), and methanol (h) over the as-prepared Co_3O_4 catalysts.

gaseous oxygen species promoted the degradation of EA. Furthermore, the high EA desorption temperatures and large desorption peak areas also confirmed the great EA adsorption ability of the C-doped samples. Figure 6f displays the CO_2 generation over the as-prepared Co_3O_4 catalysts during the TPO process. As shown in the enlarged pattern inset in Figure 6f, at the temperature below 100 °C, CO_2 generation peaks were observed in Co_3O_4−C and N−Co_3O_4−C, while Co_3O_4 and N−Co_3O_4 were not. Meanwhile, the strongest CO_2 generation peak was observed in N−Co_3O_4−C, suggesting its excellent gaseous oxygen activation ability at low temperatures. With an increase in the temperature, a large amount of CO_2 was produced. The positions of the CO_2 generation peak over Co_3O_4, Co_3O_4−C, N−Co_3O_4, and N−Co_3O_4−C were at 190, 180, 190, and 180 °C, respectively, which suggested better gaseous oxygen activation of the C-doped samples. According to the above analysis of EA adsorption, desorption, and activation results over the as-prepared Co_3O_4 catalysts, it could be concluded that the doping of C enhanced the adsorption of EA, activated gaseous oxygen species, and weakened the Co−O bond, which expedited EA degradation over the C-doped samples. Additionally, the EA breakthrough curves of the as-prepared Co_3O_4 catalysts and the corresponding adsorption capacity in the presence of 5.0 vol% H_2O, EA−TPD, and EA−

https://doi.org/10.1021/jacsau.4c01146
JACS Au 2025, 5, 363−380

TPO in the presence of 5.0 vol% H_2O were also carried out (Figure S21). The results showed that the introduction of water vapor suppressed the adsorption of EA on the catalyst surface and the activation of lattice oxygen and gaseous oxygen species, which inhibited EA degradation. However, the doping of N in N−Co_3O_4 and N−Co_3O_4−C could result in the formation of oxygen vacancies, which might interact with water vapor to produce extra active oxygen species, associatively adsorbed water species, enhancing the water resistance of N−Co_3O_4 and N−Co_3O_4−C for EA degradation. The detailed analysis is listed in Figure S21.

3.6. Degradation Intermediates and Mechanism

Generally, the thermal desorption−gas chromatography−mass spectrometer (TD−GC−MS) and in situ DRIFTS are the efficient technologies to detect the VOC degradation intermediate.[55] Therefore, the EA degradation intermediates produced over the as-prepared Co_3O_4 catalysts were determined by TD−GC−MS and in situ DRIFTS spectra. First, the gaseous intermediates generated during EA degradation over the as-prepared Co_3O_4 catalysts were detected via TD−GC−MS spectra. As shown in Figure S22, except for EA, no other degradation intermediates were detected over the as-prepared Co_3O_4 catalysts. Furthermore, the in situ DRIFTS spectra were applied to explore the surface EA degradation intermediates. Figure 7a−d presents the in situ DRIFTS spectra for EA adsorption over the as-prepared Co_3O_4 catalysts, and the assignment of the adsorption peaks is summarized in Table S8. Meanwhile, the intensity of surface-adsorbed organic species during EA adsorption over the as-prepared Co_3O_4 catalysts with time is depicted in Figure S23. As presented in Figure 7a, the adsorption peaks at 2981 and 2936 cm^{-1} were ascribed to the C−H stretching vibration of the $-CH_3$ group in EA.[56] The strong adsorption bands at 1702 and 1275 cm^{-1} were assigned to the C═O and C−O vibrations of EA, respectively.[57,58] Other peaks at 1474, 1377, 1092, and 1045 cm^{-1} were ascribed to the adsorption of EA molecules.[59,60] The presence of these peaks suggested the successful adsorption of EA on the Co_3O_4 surface. Meanwhile, the intensity of the EA adsorption peak enhanced with time. Additionally, with increasing time, some new adsorption bands at 1756 cm^{-1} (C═O stretching vibration of acetaldehyde),[61,62] 1572 cm^{-1} (asymmetric stretching vibration of COO−),[63] 1417 cm^{-1} (symmetric stretching vibration of COO−),[64] and 1156 cm^{-1} (C−O vibration of vinyl acetate)[65,66] appeared, suggesting the formation of acetaldehyde, acetate acid, and vinyl acetate during EA adsorption. These results suggested that the EA could efficiently adsorb on the catalyst surface and decompose.

Similarly, the same adsorption bands could be observed on the surface of Co_3O_4−C (Figure 7b), N−Co_3O_4 (Figure 7c), and N−Co_3O_4−C (Figure 7d) after the adsorption of EA for 60 min. However, the intensities of these adsorption peaks varies. Therefore, the intensity of EA (∼1701 cm^{-1}), acetaldehyde (∼1756 cm^{-1}), and acetate acid (∼1572 and 1417 cm^{-1}) over the as-prepared Co_3O_4 catalysts is plotted in Figures 7e−g and S23. First, for the adsorption of EA, as shown in Figures 7e and S23, EA adsorption performance over the Co_3O_4 catalysts followed the order of Co_3O_4−C > N−Co_3O_4−C > Co_3O_4 > N−Co_3O_4, which was consistent with the results of the EA breakthrough curve, further suggesting the great adsorption performance of the C-doped samples. Meanwhile, the adsorption peak intensity of EA over the C-doped samples decreased slightly after 40 min, suggesting the degradation of EA. Furthermore, the increased intermediate (acetaldehyde and acetate acid) peak intensity (Figures 7f,g and S23) also confirmed the degradation of EA during the adsorption process at 30 °C. Therefore, the in situ DRIFTS EA adsorption spectra results suggested that the C-doped samples presented the optimal adsorption performance, and the adsorbed EA could be degraded with adsorption time. Additionally, the in situ DRIFTS spectra for EA adsorption over the as-synthesized Co_3O_4 catalysts were also investigated (Figures S24 and S25) under humid conditions (5.0 vol% H_2O). The results also suggested that the introduction of water vapor greatly suppressed EA adsorption on the catalyst surface, which was consistent with the EA adsorption breakthrough curves in the humid condition (Figure S21a).

Figure 8a−d displays the in situ DRIFTS spectra of EA oxidation over the as-prepared Co_3O_4 catalysts under the condition of 1000 ppm EA + 20.0 vol% O_2 balanced with Ar at different temperatures. The assignment of the adsorbed bands related to the degradation intermediates is summarized in Table S9. For Co_3O_4, with the increase of reaction temperature, the adsorption bands at 2986, 2935, 1704, 1379, 1279, and 1046 cm^{-1}, which were assigned to the adsorption of EA, were weakened and disappeared. Meanwhile, new adsorption bands related to EA degradation intermediates were observed on the catalyst surface, such as acetaldehyde (1771 and 1757 cm^{-1}),[61,62] ethylene (1670 cm^{-1}),[65] acetate acid (1550, 1444, and 1242 cm^{-1}),[63,64,67] ethanol (1340, 1098, and 1027 cm^{-1}),[68,69] formate (1316 cm^{-1}),[61,70] vinyl acetate (1161 cm^{-1}),[65,66] and methanol (1027 cm^{-1}).[61,71] Furthermore, the adsorption peak intensity of the surface-adsorbed species is plotted in Figure S26a. The adsorption peak intensity of the intermediates increased gradually with temperature, suggesting the accumulation of EA degradation intermediates on the Co_3O_4 surface. Among these degradation intermediates, acetate acid was the dominant surface intermediate due to its intense characteristic bands, suggesting that the further degradation of acetate acid was the rate-determining step for EA oxidation.[61] Figure 8b−d presents the in situ DRIFTS spectra of EA degradation over Co_3O_4−C, N−Co_3O_4, and N−Co_3O_4−C, respectively, and the corresponding adsorption bands intensity of the intermediates is plotted in Figure S26a−d. Similar phenomena in which the intensity of EA adsorption peaks was weakened as temperature increased, accompanied by the enhancement peak intensity of the degradation intermediates (acetaldehyde, acetate acid, ethanol, formate, and methanol), were observed. Therefore, according to the results presented above, the EA degradation mechanism and pathway were obtained. First, EA was adsorbed on the catalyst surface. Then, the adsorbed EA molecules were oxidized to ethanol and acetaldehyde and further to acetate acid. After that, the C−C bond of the adsorbed acetate acid species broke to form formate and methanol and finally oxidized to CO_2 and H_2O.

To further reveal the difference of EA degradation intermediates over the as-prepared Co_3O_4 catalyst surface, the adsorption peak intensity of EA and the key intermediate species (acetate acid, formate, and methanol) is plotted in Figure 8e,f according to the in situ DRIFTS spectra. For EA, as shown in Figure 8e, as the temperature increased, EA adsorption peak intensity weakened gradually and disappeared. The disappearance of the EA adsorption band over N−Co_3O_4−C was observed at 160 °C while at 180 °C for the other three catalysts, suggesting the optimal EA degradation

https://doi.org/10.1021/jacsau.4c01146
JACS Au 2025, 5, 363−380

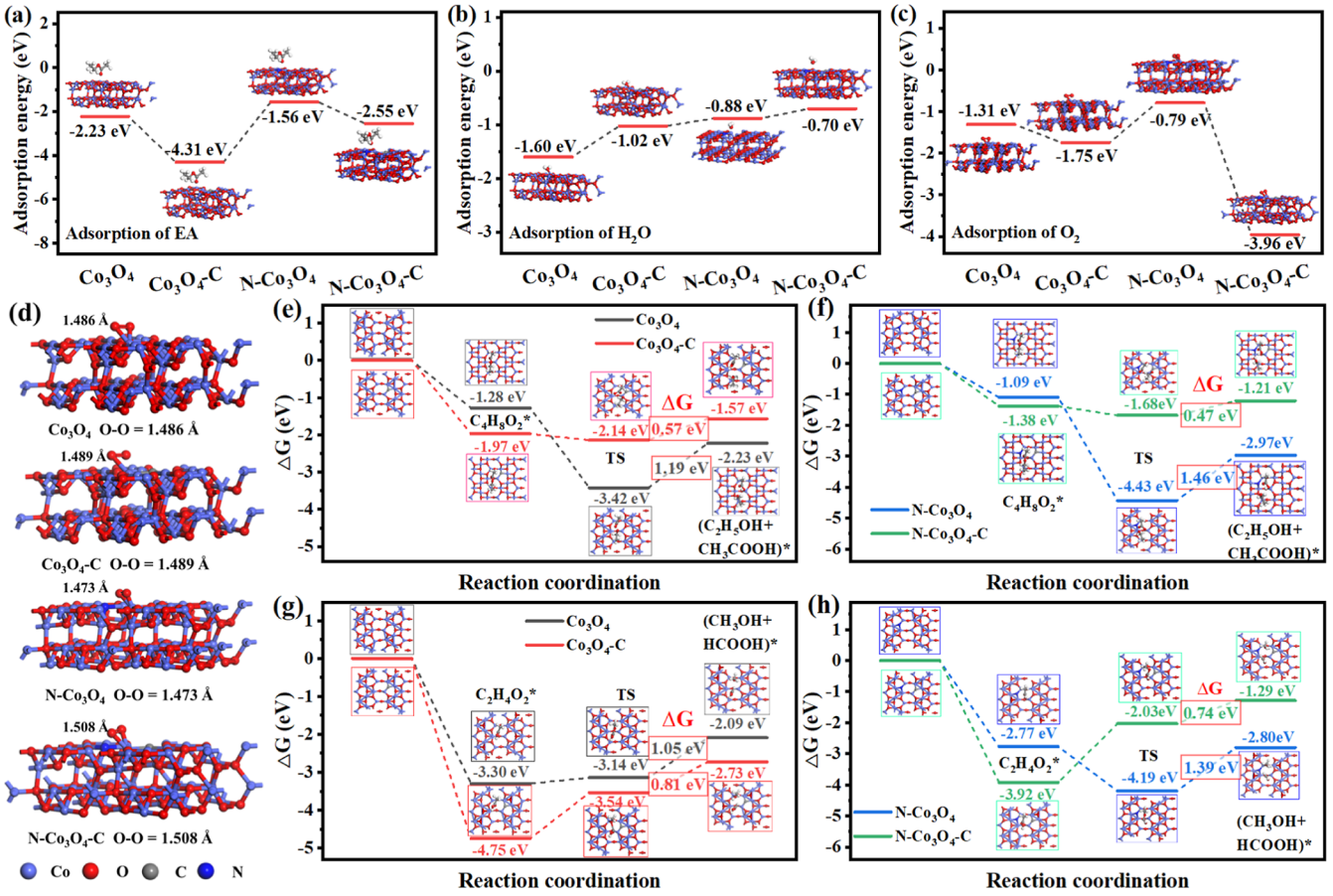

Figure 9. DFT calculations for the adsorption energy of EA (a), H_2O (b), and O_2 (c) over the Co_3O_4 catalysts and the bond length of O−O after O_2 adsorption (d); the calculated energetic routes of EA adsorption and dissociation to ethanol and acetate acid and acetate acid adsorption and dissociation to methanol and formate over Co_3O_4 and Co_3O_4−C (e,g) and N−Co_3O_4 and N−Co_3O_4−C (f,h).

performance of N−Co_3O_4−C. As shown in Figure 8f, on the surface of Co_3O_4 and N−Co_3O_4, the adsorption peak intensity of acetate acid increased gradually with temperature, while acetate acid intensity enhanced first and then weakened over Co_3O_4−C and N−Co_3O_4−C. It had been reported that the degradation of acetate acid was the rate-determining step for EA oxidation.[61] Therefore, the inferior catalytic performances of Co_3O_4 and N−Co_3O_4 might be ascribed to the occupation of surface active sites by the acetate acid species, which inhibited EA degradation. As for the C-doped samples, although the generation of acetate acid was first accumulated and then degraded over Co_3O_4−C and N−Co_3O_4−C surfaces, the different degradation temperatures were observed. Namely, the initial temperature for the decrease of acetate acid adsorption band intensity over Co_3O_4−C was observed at 180 °C while 160 °C for N−Co_3O_4−C, suggesting the easier degradation of acetate acid over the C, N-codoped N−Co_3O_4−C. Figure 8g,h plots the peak intensity of formate and methanol generated during EA oxidation. Compared with the gradual occupation of formate and acetate acid species on Co_3O_4 and N−Co_3O_4 surfaces, the intermediates on Co_3O_4−C (methanol) and N−Co_3O_4−C (formate and methanol) were first increased and then decreased, which also confirmed the better catalytic performance of the C-doped Co_3O_4−C and N−Co_3O_4−C. Notably, compared with Co_3O_4−C, acetate acid decomposition intermediates, formate and methanol, were easier to form and degrade on the N−Co_3O_4−C surface, suggesting that the breaking of the C−C bond of acetate acid and the activation of O_2 to form active oxygen species over the N−Co_3O_4−C surface were effortless. Furthermore, the easier activation of O_2 over N−Co_3O_4−C could also be confirmed by the results of TPO (Figure 6e,f). According to the results presented above, it could be inferred that the introduction of C could promote the formation of acetate acid, the key intermediate of EA, and the introduction of N enhanced the breaking of the C−C bond in acetate acid and accelerated the decomposition and oxidation of EA, namely, the rate-determining step of EA, which boosted EA degradation. Therefore, the C, N codoping of N−Co_3O_4−C presented the optimal EA degradation performance based on the synergistic effect of N, C codoping. Furthermore, the effect of water vapor on EA degradation intermediates over the as-prepared Co_3O_4 catalysts was also investigated via in situ DRIFTS (Figures S27 and S28). The results suggested that the introduction of water vapor did not influence the EA degradation pathway. Additionally, during EA degradation over Co_3O_4 and Co_3O_4−C in the presence of 5.0 vol% H_2O, the introduction of water vapor in the reaction system suppressed the activation of gaseous oxygen species, which resulted in the accumulation of the key EA degradation intermediate, acetate acid, on the catalyst surface, occupying the active sites and inhibiting EA degradation. For EA oxidation over N−Co_3O_4 and N−Co_3O_4−C, although the water vapor inhibited the activation of gaseous oxygen species, the N-doping-induced oxygen vacancies could interact with water vapor to generate extra active oxygen species (Figure 5e), which promoted the

https://doi.org/10.1021/jacsau.4c01146
JACS Au 2025, 5, 363−380

degradation of EA degradation intermediates, weakening the inhibition of H_2O on EA degradation.

3.7. Theoretical Calculations

To further investigate the EA adsorption behavior, water resistance and the O_2 adsorption energy over the as-prepared Co_3O_4 catalysts were calculated. Based on the HRTEM results, the (311) and (220) crystal faces of Co_3O_4 were exposed on the catalyst surface. Furthermore, the doping-induced defects were found in the (220) crystal face. Therefore, four model structures of Co_3O_4, Co_3O_4−C, N−Co_3O_4, and N−Co_3O_4−C with the exposed (220) crystal facet were constructed (Figure S29) to calculate the adsorption energy of EA, H_2O, and O_2 based on the density functional theory (DFT). As shown in Figure 9a, the adsorption energies of EA over Co_3O_4, Co_3O_4−C, N−Co_3O_4, and N−Co_3O_4−C were −2.23, −4.31, −1.56, and −2.55 eV, respectively, suggesting that the C-doped samples possessed the optimal EA adsorption energy, which was consistent with the TPD and TPO results. Meanwhile, the result of the EA adsorption energy further confirmed the enhancement of EA adsorption via the C-doping strategy. Figure 9b displays the H_2O adsorption energy over that of the as-prepared Co_3O_4 catalysts. The H_2O adsorption energies over Co_3O_4, Co_3O_4−C, N−Co_3O_4, and N−Co_3O_4−C were −1.60, −1.02, −0.88, and −0.70 eV, respectively. Apparently, the N-doped samples, N−Co_3O_4 and N−Co_3O_4−C, presented a low H_2O adsorption energy, which suggested that the doping of N weakened the adsorption of H_2O on the catalyst surface. As mentioned in the water-resistance test (Figure 5a−d), compared with Co_3O_4 and Co_3O_4−C, the doping of N in N−Co_3O_4 and N−Co_3O_4−C greatly enhanced their water resistance for EA degradation under humid conditions. Meanwhile, the hydrophobicity of the N-doped samples was improved (Figure 5f). Therefore, in combination with the results of the calculated H_2O adsorption energies, it could be concluded that the N doping improved the hydrophobicity and weakened the adsorption of H_2O on the catalyst surface, which enhanced the water resistance of N−Co_3O_4 and N−Co_3O_4−C for EA degradation under humid conditions.

Furthermore, the adsorption energies of O_2 over the as-prepared Co_3O_4 catalysts were also calculated, and the length of the O−O bond after adsorption was also measured. Furthermore, the longer the O−O bond, the easier the activation of the adsorbed gaseous oxygen molecules. As shown in Figure 9c, the largest O_2 adsorption energy was observed in N−Co_3O_4−C (−3.96 eV), followed by Co_3O_4−C (−1.75 eV), Co_3O_4 (−1.31 eV), and N−Co_3O_4 (−0.79 eV). Meanwhile, after adsorption, the O−O bond length (Figure 9d) over Co_3O_4, Co_3O_4−C, N−Co_3O_4, and N−Co_3O_4−C was 1.486, 1.489, 1.473, and 1.508 Å, respectively. Apparently, compared with Co_3O_4 and N−Co_3O_4, the C-doped samples presented large O_2 adsorption energies and long O−O bond lengths, especially N−Co_3O_4−C possessed the largest O_2 adsorption energy and the longest O−O bond length. This result suggested that the C, N codoping enhanced the adsorption and activation of gaseous oxygen over N−Co_3O_4−C, which was consistent with the EA degradation performance (Figure 4a) and TPO results (Figure 6f). Therefore, according to the above analysis of DFT calculation results, the enhancement of EA adsorption via C doping, the weakening of H_2O adsorption to improve the water resistance via N doping, and C, N codoping boosted the O_2 adsorption and activation could be concluded. Therefore, the synergistic effect of C, N codoping to improve the EA degradation over N−Co_3O_4−C under humid conditions could be inferred.

As mentioned in the in situ DRIFTS spectra for EA oxidation over the as-prepared Co_3O_4 catalysts (Figure 8), acetate acid was the key intermediate for EA degradation. Therefore, the adsorption and dissociation of EA molecules to form acetate acid and the adsorption and dissociation of acetate acid were calculated. To simplify the calculation, the single-layer model structure of the catalysts was used to calculate the Gibbs free energy change (ΔG). Figure 9e,f presents the ΔG of EA adsorption and dissociation [$C_4H_8O_2 \rightarrow C_4H_8O_2^* \rightarrow (CH_3CH_2O^{\bullet} + CH_3COO^{\bullet})^* \rightarrow (CH_3CH_2OH + CH_3COOH)^*$] over the as-synthesized Co_3O_4 catalysts. As shown in Figure 9e,f, the EA molecule dissociated on the surface of Co_3O_4, Co_3O_4−C, N−Co_3O_4, and N−Co_3O_4−C needed to overcome the ΔG values of 1.19, 0.57, 1.46, and 0.47 eV, respectively. This suggested the easier degradation of EA over the C-doped samples, N−Co_3O_4−C and Co_3O_4−C, followed by Co_3O_4 and N−Co_3O_4, which was consistent with the performance test (Figure 4a). Furthermore, the ΔG of acetate acid adsorption and dissociation [$C_2H_4O_2 \rightarrow C_2H_4O_2^* \rightarrow (CH_3O^{\bullet} + HCOO^{\bullet})^* \rightarrow (CH_3OH + HCOOH)^*$] over the Co_3O_4 catalysts was also calculated (Figure 9g,h). The dissociation of acetate acid over Co_3O_4, Co_3O_4−C, N−Co_3O_4, and N−Co_3O_4−C needed to overcome the ΔG values of Co_3O_4, Co_3O_4−C, N−Co_3O_4, and N−Co_3O_4−C, which were 1.05, 0.81, 1.39, and 0.74 eV, respectively. This result indicated the easier decomposition of acetate acid over N−Co_3O_4−C and Co_3O_4−C, followed by Co_3O_4 and N−Co_3O_4, which was consistent with the in situ DRIFTS spectra for EA oxidation (Figure 8). Therefore, combined with the characterizations and the DFT calculations, it could be concluded that the C doping weakened the Co−O bond and played an important role in EA and the key intermediate of EA, acetate acid, degradation.

3.8. Synergistic Effect of N, C Codoping for EA Oxidation under Humid Conditions

According to the above physical-chemical characterizations, activity tests, in situ DRIFTS spectra results, and DFT calculations, the synergistic effect of N, C codoping to enhance EA degradation over N−Co_3O_4−C was proposed. First, the doping of C weakened the Co−O bond (Figures 1b and 3f) and increased the surface area (Figure S4), which improved the reducibility, mobility, and activation of the lattice oxygen species (Figure 3g,h) and the adsorption of EA (Figures 6, 7, and 9a). Meanwhile, the adsorbed EA was dissociated to form ethanol and acetaldehyde, which were further oxidized to acetate acid (key intermediate) accumulated on the catalyst surface (Figures 7 and 8). Then, the doping of N in N−Co_3O_4−C further boosted the reducibility (Figure 3g) of the N, C-codoped catalyst, increased the surface oxygen vacancies concentration, improved the hydrophobicity, weakened the adsorption of water vapor on the catalyst surface (Figure 9b), and promoted the adsorption and activation of gaseous oxygen species (Figure 9c,d). Meanwhile, the interaction between surface oxygen vacancies and water vapor could induce the formation of extra active oxygen species, associatively water species, which improved the water resistance (Figure 5) and the cleavage of the C−C bond in acetate acid, promoting EA degradation (Figure 8). Based on the analysis presented above and the results of in situ DRIFTS spectra, the mechanism of the synergistic effect of N, C codoping to boost EA

https://doi.org/10.1021/jacsau.4c01146
JACS Au 2025, 5, 363−380

degradation and the EA degradation pathway are summarized in Scheme 1. As shown in Scheme 1, first, the EA molecules

Scheme 1. Catalytic Synergistic Effect Mechanism of N, C Codoping in N−Co_3O_4−C Catalysts for EA Degradation

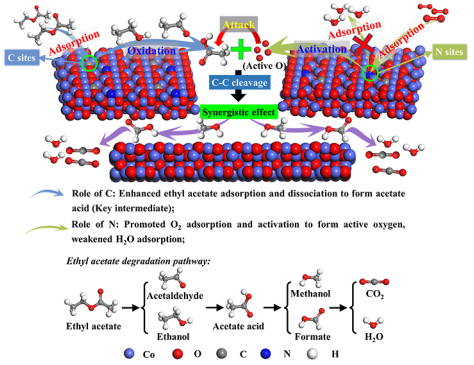

were absorbed on the C sites in the catalyst surface and oxidized to ethanol, acetaldehyde, and further to acetate acid. Then, N sites adsorbed and activated gaseous oxygen molecules to form active oxygen species, which would attack the C−C bond of acetate acid to generate methanol and formate, accelerating the degradation of EA. Under the synergistic effect of N and C, EA was rapidly degraded on N−Co_3O_4−C.

4. CONCLUSIONS

In summary, the C, N-codoped N−Co_3O_4−C catalyst was successfully prepared via a simple hydrothermal-calcination method and applied for the catalytic degradation of EA. Compared with the undoped and C- or N-doped catalysts, the C, N-codoped sample presented optimal EA degradation performance (T_{90} = 177 °C) and water resistance (5.0 vol%). The N−Co_3O_4−C catalyst demonstrated great low-temperature redox ability, more surface Co^{3+} and O_{ads} species, and better lattice species mobility. Additionally, characterization and DFT calculation results suggested that the C doping weakened the strength of the Co−O bond and increased the surface area, resulting in the enhancement of lattice oxygen species activation and mobility. The doping of N improved the hydrophobicity, weakened the adsorption of water vapor on the catalyst surface, and improved the adsorption and activation of gaseous oxygen species, leading to great water resistance and the deep oxidation of the key intermediates. Importantly, in situ DRIFTS results exhibited that the doped C sites adsorbed and dissociated EA molecules to form ethanol and acetaldehyde species, which were further oxidized to acetate acid by the lattice oxygen species and accumulated on the catalyst surface. Subsequently, the N sits on the catalyst surface, adsorbing and activating gaseous oxygen species to form active oxygen species, which attacked and broke the C−C bonds of acetate acid species to accelerate the deep oxidation of EA. Therefore, the improvement of EA catalytic performance over the C, N-codoped N−Co_3O_4−C catalyst for EA degradation was the result of the synergistic effect of C and N codoping. This work provided a new strategy for the preparation of high-performance catalysts via C,N codoping for low-temperature VOC degradation under humid conditions.

ASSOCIATED CONTENT

Supporting Information

The Supporting Information is available free of charge at https://pubs.acs.org/doi/10.1021/jacsau.4c01146.

Details of the catalyst preparation, characterization, catalytic performance tests, and some results of characterization (PDF)

AUTHOR INFORMATION

Corresponding Author

Xiaodong Zhang − *School of Environment and Architecture, University of Shanghai for Science and Technology, Shanghai 200093, China; Shanghai Non-carbon Energy Conversion and Utilization Institute, Shanghai 200240, China;* orcid.org/0000-0003-2217-6173; Phone: + 86 15921267160; Email: fatzhxd@126.com; Fax: + 86 021 55275979

Authors

Fukun Bi − *School of Environment and Architecture, University of Shanghai for Science and Technology, Shanghai 200093, China; School of Health Science and Engineering, University of Shanghai for Science and Technology, Shanghai 200093, China;* orcid.org/0000-0003-0115-2826

Jiafeng Wei − *School of Environment and Architecture, University of Shanghai for Science and Technology, Shanghai 200093, China*

Zhuoxuan Zhou − *School of Environment and Architecture, University of Shanghai for Science and Technology, Shanghai 200093, China*

Yaofei Zhang − *School of Environment and Architecture, University of Shanghai for Science and Technology, Shanghai 200093, China*

Bin Gao − *School of Environment and Architecture, University of Shanghai for Science and Technology, Shanghai 200093, China*

Ning Liu − *School of Environment and Architecture, University of Shanghai for Science and Technology, Shanghai 200093, China; Shanghai Non-carbon Energy Conversion and Utilization Institute, Shanghai 200240, China;* orcid.org/0000-0001-7600-4233

Jingcheng Xu − *School of Materials and Chemistry, University of Shanghai for Science and Technology, Shanghai 200093, China*

Baolin Liu − *School of Health Science and Engineering, University of Shanghai for Science and Technology, Shanghai 200093, China*

Yuandong Huang − *School of Environment and Architecture, University of Shanghai for Science and Technology, Shanghai 200093, China*

Complete contact information is available at: https://pubs.acs.org/10.1021/jacsau.4c01146

Author Contributions

CRediT: **Fukun Bi** data curation, formal analysis, funding acquisition, writing - original draft; **Jiafeng Wei** data curation, investigation, software; **Zhuoxuan Zhou** data curation, investigation, methodology; **Yaofei Zhang** data curation, investigation, software; **Bin Gao** investigation, methodology; **Ning Liu** supervision, validation, visualization; **Jingcheng Xu** methodology, software; **Baolin Liu** supervision, visualization;

https://doi.org/10.1021/jacsau.4c01146
JACS Au 2025, 5, 363−380

Yuandong Huang supervision, visualization; **Xiaodong Zhang** funding acquisition, project administration, writing - review & editing.

Notes

The authors declare no competing financial interest.

■ ACKNOWLEDGMENTS

This work was sponsored financially by the National Natural Science Foundation of China (No. 12175145) and the Shanghai Rising-Star Program (24YF2729800).

■ REFERENCES

(1) Bi, F. K.; Zhao, Z. Y.; Yang, Y.; Gao, W. K.; Liu, N.; Huang, Y. D.; Zhang, X. D. Chlorine-Coordinated Pd Single Atom Enhanced the Chlorine Resistance for Volatile Organic Compound Degradation: Mechanism Study. *Environ. Sci. Technol.* **2022**, *56*, 17321−17330.

(2) Han, W. G.; Ling, W. T.; Gao, P.; Dong, F.; Tang, Z. C. Engineering Pt Single Atom Catalyst with Abundant Lattice Oxygen by Dual Nanospace Confinement Strategy for The Efficient Catalytic Elimination of VOCs. *Appl. Catal., B* **2024**, *345*, 123687.

(3) Wang, X.; Wu, L. K.; Wang, Z. W.; Feng, Y.; Liu, Y. X.; Dai, H. X.; Wang, Z. H.; Deng, J. G. Photothermal Synergistic Catalytic Oxidation of Ethyl Acetate over MOFs-Derived Mesoporous N-TiO_2 Supported Pd Catalysts. *Appl. Catal., B* **2023**, *322*, 122075.

(4) Bi, F. K.; Wei, J. F.; Gao, B.; Liu, N.; Xu, J. C.; Liu, B. L.; Huang, Y. D.; Zhang, X. D. New Insight into the Antagonism Mechanism Between Binary VOCs During Their Degradation over Pd/ZrO_2 Catalysts. *ACS EST Engg.* **2024**, *4*, 1346−1355.

(5) Zhao, Q. Y.; Zhao, Z. Y.; Rao, R. Z.; Yang, Y.; Ling, S. Y.; Bi, F. K.; Shi, X. Y.; Xu, J. C.; Lu, G.; Zhang, X. D. Universitetet i Oslo-67 (UiO-67)/Graphite Oxide Composites with High Capacities of Toluene: Synthesis Strategy and Adsorption Mechanism Insight. *J. Colloid Interface Sci.* **2022**, *627*, 385−397.

(6) Zhang, X. D.; Ma, S. T.; Gao, B.; Bi, F. K.; Liu, Q. H.; Zhao, Q. Y.; Xu, J. C.; Lu, G.; Yang, Y. Q.; Wu, M. H. Effect of Benzoic Acid and Dopamine Hydrochloride as A Modulator in the Water Resistance of Universitetet i Oslo-67: Adsorption Performance and Mechanism. *J. Colloid Interface Sci.* **2023**, *651*, 424−435.

(7) Huang, J. H.; Wei, J. F.; Tian, F. Y.; Bi, F. K.; Rao, R. Z.; Wang, Y. X.; Tao, H. C.; Liu, N.; Zhang, X. D. Nitrogen-induced TiO_2 electric field polarization for efficient photodegradation of high-concentration ethyl acetate: Mechanisms and reaction pathways. *Mater. Today Chem.* **2024**, *41*, 102292.

(8) Zhang, X. D.; Gao, B.; Rao, R. Z.; Bi, F. K.; Li, C. Y.; Yue, K.; Wang, Y. X.; Xu, J. C.; Feng, X. B.; Yang, Y. Q. Defects Materials of Institut Lavoisier-125(Ti) Materials Enhanced Photocatalytic Activity for Toluene and Chlorobenzene Mixtures Degradation: Mechanism Study. *J. Colloid Interface Sci.* **2024**, *660*, 423−439.

(9) Huang, J. H.; Feng, X. B.; Bi, F. K.; Huang, G. H.; Rao, R. Z.; Qiao, R.; Zhang, X. D. Strategic defect engineering in TiO_2 catalysts through electron beam irradiation: Unraveling enhanced photocatalytic pathways for multicomponent VOCs degradation. *Sep. Purif. Technol.* **2025**, *359*, 130804.

(10) Bo, Z.; Cao, M. Y.; Zhang, H. H.; Wang, Y. L.; Yan, J. H.; Cen, K. F.; Ostrikov, K.; Tu, X. Enhancing Plasma-Catalytic Toluene Oxidation: Unraveling the Role of Lewis-Acid Sites on δ-MnO_2. *Chem. Eng. J.* **2024**, *481*, 148399.

(11) Yang, Y.; Zhao, S. H.; Bi, F. K.; Chen, J. F.; Li, Y. T.; Cui, L. F.; Xu, J. C.; Zhang, X. D. Oxygen-Vacancy-Induced O_2 Activation and Electron-Hole Migration Enhance Photothermal Catalytic Toluene Oxidation. *Cell Rep. Phys. Sci.* **2022**, *3*, 101011.

(12) Lu, Z. H.; Guo, L.; Shen, Q. Y.; Bi, F. K.; Li, C. Y.; Zhang, X. D. The Application of Metal-Organic Frameworks and Their Derivatives in the Catalytic Oxidation of Typical Gaseous Pollutants: Recent Progress and Perspective. *Sep. Purf. Technol.* **2024**, *340*, 126772.

(13) Bi, F. K.; Feng, X. B.; Zhou, Z. X.; Zhang, Y. F.; Wei, J. F.; Yuan, L. Y. M.; Liu, B. L.; Huang, Y. D.; Zhang, X. D. Mn-Based Catalysts Derived from The Non-Thermal Treatment of Mn-MIL-100 to Enhance Its Water-Resistance for Toluene Oxidation: Mechanism Study. *Chem. Eng. J.* **2024**, *485*, 149776.

(14) Lu, Z. H.; Guo, L.; Bi, F. K.; Ma, S. T.; Shen, Q. Y.; Qiao, R.; Zhang, X. D. Insight into the degradation mechanism of mixed VOCs oxidation over Pd/UiO-66(Ce) catalysts: Combination of operando spectroscopy and theoretical calculation. *Sep. Purif. Technol.* **2025**, *354*, 129443.

(15) Gao, B.; Bi, F. K.; Zhou, Z. X.; Zhang, Y. F.; Wei, J. F.; Lv, X. T.; Liu, B. L.; Huang, Y. D.; Zhang, X. D. A Bimetallic MOF-Derived MnCo Spinel Oxide Catalyst to Enhance Toluene Catalytic Degradation. *Chem. Commun.* **2024**, *60*, 7455−7458.

(16) Bi, F. K.; Wei, J. F.; Gao, B.; Ma, S. T.; Liu, N.; Xu, J. C.; Liu, B. L.; Huang, Y. D.; Zhang, X. D. How the Most Neglected Residual Species in MOF-Based Catalysts Involved in Catalytic Reactions to Form Toxic Byproducts. *Environ. Sci. Technol.* **2024**, *58*, 19797−19806.

(17) Bi, F. K.; Ma, S. T.; Gao, B.; Liu, B. L.; Huang, Y. D.; Qiao, R.; Zhang, X. D. Boosting Toluene Deep Oxidation by Tuning Metal-Support Interaction in MOF-Derived Pd@ZrO_2 Catalysts: The Role of Interfacial Interaction Between Pd and ZrO_2. *Fuel* **2024**, *357*, 129833.

(18) Zhang, X. D.; Xiang, S.; Du, Q. X.; Bi, F. K.; Xie, K. L.; Wang, L. Effect of Calcination Temperature on the Structure and Performance of Rod-Like MnCeOx Derived from MOFs Catalysts. *Mol. Catal.* **2022**, *522*, 112226.

(19) Ma, Y.; Wang, L.; Ma, J. Z.; Liu, F. D.; Einaga, H.; He, H. Improved and Reduced Performance of Cu- and Ni-Substituted Co_3O_4 Catalysts with Varying Co_{Oh}/Co_{Td} and Co^{3+}/Co^{2+} Ratios for The Complete Catalytic Oxidation of VOCs. *Environ. Sci. Technol.* **2022**, *56*, 9751−9761.

(20) Li, R.; Shi, X. J.; Huang, Y.; Chen, M. J.; Zhu, D. D.; Ho, W. K.; Cao, J. J.; Lee, S. C. Catalytic Oxidation of Formaldehyde on Ultrathin Co_3O_4 Nanosheets at Room Temperature: Effect of Enhanced Active Sites Exposure on Reaction Path. *Appl. Catal., B* **2022**, *319*, 121902.

(21) Ma, Y.; Wang, L.; Ma, J. Z.; Wang, H. H.; Zhang, C. B.; Deng, H.; He, H. Investigation into The Enhanced Catalytic Oxidation of o-Xylene over MOF-Derived Co_3O_4 with Different Shapes: The Role of Surface Twofold-Coordinate Lattice Oxygen (O_{2f}). *ACS Catal.* **2021**, *11*, 6614−6625.

(22) Chen, Y. Y.; Zhang, Z.; Wang, X.; Lin, Y. D.; Zuo, J. C.; Yang, X. H.; Chen, S. H.; Luo, Y. J.; Qian, Q. R.; Chen, Q. H. Crystal Plane Effect of Co_3O_4 on Styrene Catalytic Oxidation: Insights into The Role of Co^{3+} and Oxygen Mobility at Diverse Temperatures. *ACS Appl. Mater. Interfaces* **2023**, *15*, 32404−32415.

(23) Chen, X.; Yu, S. N.; Liu, W.; Zhang, S. N.; Liu, S. C.; Feng, Y.; Zhang, X. J. Recent Advance on Cobalt-Based Oxide for The Catalytic Removal of Volatile Organic Compounds: A Review. *Res. Chem. Mater.* **2022**, *1*, 27−46.

(24) Li, Y.; Li, K.; Wang, Y. H.; Zhou, K.; Zhao, M. Q.; Hu, M. M.; Liu, Y. Q.; Qin, L. P.; Cui, B. Fe-Doped Porous Co_3O_4 Nanosheets with Highly Efficient Catalytic Performance for Soot Oxidation. *Chem. Eng. J.* **2022**, *431*, 133248.

(25) Bae, J.; Shin, D.; Jeong, H.; Choe, C.; Choi, Y.; Han, J. W.; Lee, H. Facet-Dependent Mn Doping on Shaped Co_3O_4 Crystals for Catalytic Oxidation. *ACS Catal.* **2021**, *11*, 11066−11074.

(26) Ma, L.; Seo, C. Y.; Chen, X. Y.; Sun, K.; Schwank, J. W. Indium-Doped Co_3O_4 Nanorods for Catalytic Oxidation of CO and C_3H_6 Towards Diesel Exhaust. *Appl. Catal., B* **2018**, *222*, 44−58.

(27) Sun, L. T.; Liang, X. L.; Liu, H. M.; Cao, H. J.; Liu, X. H.; Jin, Y.; Li, X. Y.; Chen, S.; Wu, X. D. Activation of Co-O Bond in (110) Facet Exposed Co_3O_4 by Cu Doping for The Boost of Propane Catalytic Oxidation. *J. Hazard. Mater.* **2023**, *452*, 131319.

(28) Hu, X. B.; Wang, Y. Z.; Wu, R. F.; Zhao, Y. X. N-Doped Co_3O_4 Catalyst with A High Efficiency for The Catalytic Decomposition of N_2O. *Mol. Catal.* **2021**, *509*, 111656.

(29) Wang, Z. C.; Xu, W. J.; Chen, X. K.; Peng, Y. H.; Song, Y. Y.; Lv, C. X.; Liu, H. L.; Sun, J. W.; Yuan, D.; Li, X. Y.; Guo, X. X.; Yang,

https://doi.org/10.1021/jacsau.4c01146
JACS Au 2025, 5, 363−380

D. J.; Zhang, L. X. Defect-Rich Nitrogen Doped Co_3O_4/C Porous Nanocubes Enable High-Efficiency Bifunctional Oxygen Electrocatalysis. *Adv. Funct. Mater.* **2019**, *29*, 1902875.
(30) Yan, C. S.; Zhu, Y.; Li, Y. T.; Fang, Z. W.; Peng, L. L.; Zhou, X.; Chen, G.; Yu, G. H. Local Built-in Electric Field Enabled in Carbon-Doped Co_3O_4 Nanocrystals for Superior Lithium-Ion Storage. *Adv. Funct. Mater.* **2018**, *28*, 1705951.
(31) Zhong, J. P.; Zeng, Y. K.; Chen, D. D.; Mo, S. P.; Zhang, M. Y.; Fu, M. L.; Wu, J. L.; Su, Z. X.; Chen, P. R.; Ye, D. Q. Toluene Oxidation over Co^{3+}-Rich Spinel Co_3O_4: Evaluation of Chemical and By-Product Species Identified By In Situ DRIFTS Combined with PTR-TOF-MS. *J. Hazard. Mater.* **2020**, *386*, 121957.
(32) Han, D. W.; Ma, X. Y.; Yang, X. Q.; Xiao, M. L.; Sun, H.; Ma, L. J.; Yu, X. L.; Ge, M. F. Metal Organic Framework-Templated Fabrication of Exposed Surface Defect-Enriched Co_3O_4 Catalysts for Efficient Toluene Oxidation. *J. Colloid Interface Sci.* **2021**, *603*, 695−705.
(33) Liu, B.; Li, C.; Zhang, G.; Yao, X.; Chuang, S. S. C.; Li, Z. Oxygen Vacancy Promoting Dimethyl Carbonate Synthesis from CO_2 and Methanol over Zr-Doped CeO_2 Nanorods. *ACS Catal.* **2018**, *8*, 10446−10456.
(34) Zhong, J. P.; Zeng, Y. K.; Zhang, M. Y.; Feng, W. H.; Xiao, D. R.; Wu, J. L.; Chen, P. R.; Fu, M. L.; Ye, D. Q. Toluene Oxidation Process and Proper Mechanism over Co_3O_4 Nanotubes: Investigation Through In-Iitu DRIFTS Combined with PTR-TOF-MS and Quasi In-Situ XPS. *Chem. Eng. J.* **2020**, *397*, 125375.
(35) Mu, G. Y.; Zeng, Y.; Cao, Y. N.; Liu, F. J.; Liang, S. J.; Zhan, Y. Y.; Jiang, L. L. Oxygen vacancy defects engineering on Cu-doped Co_3O_4 for promoting effective COS hydrolysis. *Green Energy Environ.* **2023**, *8*, 831−841.
(36) Shen, Y. J.; Deng, J.; Impeng, S.; Li, S. X.; Yan, T. T.; Zhang, J. P.; Shi, L. Y.; Zhang, D. S. Boosting Toluene Combustion by Engineering Co-O Strength in Cobalt Oxide Catalysts. *Environ. Sci. Technol.* **2020**, *54*, 10342−10350.
(37) Yin, C. C.; Liu, Y. N.; Xia, Q. N.; Kang, S. F.; Li, X.; Wang, Y.; Cui, L. Oxygen Vacancy-Rich Nitrogen-Doped Co_3O_4 Nanosheets as An Efficient Water-Resistant Catalyst for Low Temperature CO Oxidation. *J. Colloid Interface Sci.* **2019**, *553*, 427−435.
(38) Qin, X. C.; Xue, Q.; Su, C. L.; Dang, Y.; Sun, X. Q.; Zhou, Y. Z. Oxygen Vacancies-Enriched Porous CeO_2-Co_3O_4 Hybrid Nanosheets for High-Efficiency Toluene Catalytic Oxidation. *J. Environ. Chem. Eng.* **2024**, *12*, 112685.
(39) Raimundo, R. A.; Silva, J. N.; Silva, T. R.; Araujo, A. J. M.; Oliveira, J. F. G. A.; de Lima, L. C.; Morales, M. A.; Soares, M. M.; Macedo, D. A. Green Chemistry Synthesis of Co_3O_4-CoO Nanocomposite and Electrochemical Assessment for Oxygen Evolution Reaction. *Mater. Lett.* **2023**, *341*, 134196.
(40) Bi, F. K.; Wei, J. F.; Ma, S. T.; Zhao, Q. Y.; Zhang, J. R.; Qiao, R.; Xu, J. C.; Liu, B. L.; Huang, Y. D.; Zhang, X. D. Fluorination Modification Enhanced The Water Resistance of Universitetet i Oslo-67 for Multiple Volatile Organic Compounds Adsorption under High Humidity Conditions: Mechanism Study. *J. Colloid Interface Sci.* **2024**, *665*, 898−910.
(41) Bi, F. K.; Zhang, Y. F.; Zhou, Z. X.; Liu, B. L.; Huang, Y. D.; Wang, L.; Qin, Y.; Zhang, X. D. Mn-MIL-100 Non-Thermally Derived MnOx Catalysts for Toluene Oxidation. *Mater. Lett.* **2024**, *358*, 135888.
(42) Wang, H. Q.; Wu, Z. B.; Liu, Y. A Simple Two-Step Template Approach for Preparing Carbon-Doped Mesoporous TiO_2 Hollow Microspheres. *J. Phys. Chem. C* **2009**, *113*, 13317−13324.
(43) Yan, C. S.; Chen, G.; Zhou, X.; Sun, J. X.; Lv, C. D. Template-Based Engineering of Carbon-Doped Co_3O_4 Hollow Nanofibers as Anode Materials for Lithium-Ion Batteries. *Adv. Funct. Mater.* **2016**, *26*, 1428−1436.
(44) Shen, Q. Y.; Lu, Z. H.; Bi, F. K.; Zhang, D. F.; Li, L. J.; Zhang, X. D.; Yang, Y. Q.; Wu, M. H. Regulating Electronic Metal-Support Interaction by Synthetic Methods to Enhance the Toluene Degradation over Pt/Co_3O_4 Catalysts. *Sep. Purf. Technol.* **2023**, *325*, 124707.
(45) Li, R.; Huang, Y.; Shi, X. J.; Wang, L. Q.; Li, Z. Y.; Zhu, D. D.; Liang, X. L.; Cao, J. J.; Xiong, Y. J. Dopant Site Engineering on 2D Co_3O_4 Enables Enhanced Toluene Oxidation in a Wide Temperature Range. *Environ. Sci. Technol.* **2023**, *57*, 13236−13246.
(46) Xiao, M. L.; Yu, X. L.; Guo, Y. C.; Ge, M. F. Boosting Toluene Combustion by Tuning Electronic Metal-Support Interactions in In Situ Grown Pt@Co_3O_4 Catalysts. *Environ. Sci. Technol.* **2022**, *56*, 1376−1385.
(47) Li, R.; Huang, Y.; Zhu, Y. M.; Guo, M. Z.; Peng, W.; Zhi, Y. Z.; Wang, L. Q.; Cao, J. J.; Lee, S. C. Enhancing Oxygen Activation Ability by Composite Interface Construction over a 2D Co_3O_4-Based Monolithic Catalyst for Toluene Oxidation. *Environ. Sci. Technol.* **2024**, *58*, 14906−14917.
(48) Liu, R.; Chu, Y. T.; Li, Y. M.; Li, K. J.; Li, T.; Yu, H. B.; Liang, R.; Chen, Y. P.; Wu, T.; Yin, H. F. Facet Effect on Nanosheet Co_3O_4 Catalysts for Toluene Oxidation: Decisive Role of Co^{3+} and Reaction-Induced Oxygen Vacancy. *J. Environ. Chem. Eng.* **2024**, *12*, 112640.
(49) Rabee, A. I.; Gaid, C. B.; Mekhemer, G. A.; Zaki, M. I. Combined TPR, XRD, and FTIR Studies on The Reduction Behavior of Co_3O_4. *Mater. Chem. Phys.* **2022**, *289*, 126367.
(50) Hou, Z. Q.; Chen, M. Q.; Liu, Y. X.; Deng, J. G.; Jing, L.; Gao, R. Y.; Pei, W. B.; Li, Z. Y.; Dai, H. X. Enhanced Moisture Resistance and Catalytic Stability of Ethylene Oxidation at Room Temperature by the Ultrasmall MnOx Cluster/Pt Hetero-Junction. *Appl. Catal., B* **2023**, *339*, 123115.
(51) Wang, J.; Zhang, P.; Li, J.; Jiang, C.; Yunus, R.; Kim, J. Room-Temperature Oxidation of Formaldehyde by Layered Manganese Oxide: Effect of Water. *Environ. Sci. Technol.* **2015**, *49*, 12372−12379.
(52) Yang, H.; Ma, C. Y.; Zhang, X.; Li, Y.; Cheng, J.; Hao, Z. Understanding the Active Sites of Ag/Zeolites and Deactivation Mechanism of Ethylene Catalytic Oxidation at Room Temperature. *ACS Catal.* **2018**, *8*, 1248−1258.
(53) Pei, D. N.; Gong, L.; Zhang, A. Y.; Zhang, X.; Chen, J. J.; Mu, Y.; Yu, H. Q. Defective Titanium Dioxide Single Crystals Exposed by High-Energy {001} Facets for Efficient Oxygen Reduction. *Nat. Commun.* **2015**, *6*, 8696.
(54) Gao, Z.; Wang, J. X.; Muhammad, Y.; Zhang, Y. B.; Shah, S. J.; Hu, Y.; Chu, Z.; Zhao, Z. X.; Zhao, Z. Enhanced Moisture-Resistance and Excellent Photocatalytic Performance of Synchronous N/Zn-Decorated MIL-125(Ti) for Vaporous Acetaldehyde Degradation. *Chem. Eng. J.* **2020**, *388*, 124389.
(55) Zhao, Z. Y.; Ma, S. T.; Gao, B.; Bi, F. K.; Qiao, R.; Yang, Y.; Wu, M. H.; Zhang, X. D. A Systematic Review of Intermediates and Their Characterization Methods in VOCs Degradation by Different Catalytic Technologies. *Sep. Purif. Technol.* **2023**, *314*, 123510.
(56) Pan, T. T.; Deng, H.; Lu, Y. Q.; Ma, J. Z.; Wang, L.; Zhang, C. B.; He, H. Synergistic Catalytic Oxidation of Typical Volatile Organic Compound Mixtures on Mn-Based Catalysts: Significant Promotion Effect and Reaction Mechanism. *Environ. Sci. Technol.* **2023**, *57*, 1123−1133.
(57) Galle, T.; Van Lagen, B.; Kurtenbach, A.; Bierl, R. An FTIR-DRIFT Study on River Sediment Particle Structure: Implications for Biofilm Dynamics and Pollutant Binding. *Environ. Sci. Technol.* **2004**, *38*, 4496−4502.
(58) Ma, M. D.; Yang, R.; Jiang, Z. Y.; Chen, C. W.; Liu, Q. Y.; Albilali, R.; He, C. Fabricating M/Al_2O_3/Cordierite (M = Cr, Mn, Fe, Co, Ni and Cu) Monolithic Catalysts for Ethyl Acetate Efficient Oxidation: Unveiling The Role of Water Vapor and Reaction Mechanism. *Fuel* **2021**, *303*, 121244.
(59) Sundaraganesan, N.; Meganathan, C.; Karthikeyan, B. F. T.-I. R. FT-Raman Spectra and Quantum Chemical Calculations of Some Chloro Substituted Phenoxy Acetic Acids. *Spectrochim. Acta* **2008**, *70*, 430−438.
(60) Zhang, W.; Innocenti, G.; Ferbinteanu, M.; Ramos-Fernandez, E. V.; Sepulveda-Escribano, A.; Wu, H.; Cavani, F.; Rothenberg, G.; Shiju, N. R. Understanding the Oxidative Dehydrogenation of Ethyl Lactate to Ethyl Pyruvate over Vanadia/Titania. *Catal. Sci. Technol.* **2018**, *8*, 3737−3747.

https://doi.org/10.1021/jacsau.4c01146
JACS Au 2025, 5, 363−380

(61) Mo, S. P.; Zhao, X.; Huang, L. L.; Zhou, J. J.; Li, S. D.; Peng, R. S.; Tu, Z. H.; Liao, L.; Xie, Q. L.; Chen, Y. F.; Zhang, Y. N.; Ye, D. Q. Uncovering The Role of Unsaturated Coordination Defects in Manganese Oxides for Concentrated Solar-Heating Photothermal OVOCs Oxidation: Experimental and DFT Explorations. *Appl. Catal., B* **2024**, *342*, 123435.
(62) Yang, Y.; Li, Y.; Zhang, Q.; Zeng, M.; Wu, S.; Lan, L.; Zhao, X. Novel Photoactivation and Solar-Light-Driven Thermocatalysis on ε-MnO_2 Nanosheets Lead to Highly Efficient Catalytic Abatement of Ethyl Acetate without Acetaldehyde as Unfavorable By-Product. *J. Mater. Chem. A* **2018**, *6*, 14195−14206.
(63) Dong, N.; Ye, Q.; Zhang, D.; Xiao, Y.; Dai, H. Reduced Graphene Oxide as An Effective Promoter to The Layered Manganese Oxide-Supported Ag Catalysts for The Oxidation of Ethyl Acetate and Carbon Monoxide. *J. Hazard. Mater.* **2022**, *431*, 128518.
(64) Dong, N.; Chen, M.; Ye, Q.; Zhang, D.; Dai, H. An Investigation on Catalytic Performance and Reaction Mechanisms of Fe/OMS-2 for The Oxidation of Carbon Monoxide, Ethyl Acetate, and Toluene. *J. Environ. Sci.* **2022**, *112*, 258−268.
(65) Ma, M. D.; Yang, R.; He, C.; Jiang, Z. Y.; Shi, J. W.; Albilali, R.; Fayaz, K.; Liu, B. J. Pd-Based Catalysts Promoted by Hierarchical Porous Al_2O_3 and ZnO Microsphere Supports/Coatings for Ethyl Acetate Highly Active and Stable Destruction. *J. Hazard. Mater.* **2021**, *401*, 123281.
(66) Haque, M. M.; Puglia, D.; Fortunati, E.; Pracella, M. Effect of Reactive Functionalization on Properties and Degradability of Poly(Lactic Acid)/Poly(Vinyl Acetate) Nanocomposites with Cellulose Nanocrystals. *React. Funct. Polym.* **2017**, *110*, 1−9.
(67) Ye, Y. C.; Xu, J.; Gao, L. J.; Zang, S. H.; Chen, L. Q.; Wang, L. H.; Mo, L. Y. CuO/CeO_2 Catalysts Prepared by Modified Impregnation Method for Ethyl Acetate Oxidation. *Chem. Eng. J.* **2023**, *471*, 144667.
(68) Li, J.; Mo, S.; Ding, X.; Huang, L.; Zhou, X.; Fan, Y.; Zhang, Y.; Fu, M.; Xie, Q.; Ye, D. Hollow Cavity Engineering of MOFs-Derived Hierarchical MnO_x Structure for Highly Efficient Photothermal Degradation of Ethyl Acetate under Light irradiation. *Chem. Eng. J.* **2023**, *464*, 142412.
(69) Sun, Y. L.; Liu, P. X.; Wang, Z. H.; Tang, H. R.; He, Y.; Zhu, Y. Q. Efficient Catalytic Ozonation of Ethyl Acetate over Cu-Mn Catalysts: Further Insights into The Reaction Mechanism. *Chem. Eng. J.* **2023**, *477*, 147282.
(70) Huttunen, P. K.; Labadini, D.; Hafiz, S. S.; Gokalp, S.; Wolff, E. P.; Martell, S. M.; Foster, M. DRIFTS Investigation of Methanol Oxidation on CeO_2 Nanoparticles. *Appl. Surf. Sci.* **2021**, *554*, 149518.
(71) Shen, Z.; Gao, E.; Meng, X.; Xu, J.; Sun, Y.; Zhu, J.; Li, J.; Wu, Z.; Wang, W.; Yao, S.; Dai, Q. Mechanistic Insight into Catalytic Combustion of Ethyl Acetate on Modified CeO_2 Nanobelts: Hydrolysis-Oxidation Process and Shielding Effect of Acetates/Alcoholates. *Environ. Sci. Technol.* **2023**, *57*, 3864−3874.

https://doi.org/10.1021/jacsau.4c01146
JACS Au 2025, 5, 363−380